Tellus (1987), *39A*, 272–306

Research aircraft measurements of a polar low over the Norwegian Sea

By M. A. SHAPIRO, L. S. FEDOR and TAMARA HAMPEL,
NOAA/ERL/Wave Propagation Laboratory, Boulder, Colorado 80303, USA

(Manuscript received 23 May; in final form 22 December 1986)

ABSTRACT

On 27 February 1984, the Arctic Cyclone Expedition carried out the first research aircraft measurements within a polar low. The low developed over the Norwegian Sea south of Jan Mayen in response to the baroclinic forcing by an eastward propagating upper-level synoptic-scale short wave. Observations from the NOAA WP-3D research aircraft documented the three-dimensional distribution of wind, temperature, moisture, and precipitation within the low. The polar low had a warm inner core and maximum surface winds of ~ 35 m s^{-1}. Heavy meso-convective precipitation was encountered within a frontal-like, mesoscale, baroclinic shear zone that spiraled into the low center from its southwestern quadrant. Vorticity and divergence values within the front reached 25×10^{-4} s^{-1} and 13×10^{-4} s^{-1}, respectively, where the frontal width narrowed to 10 km near the sea surface. Radar reflectivities exceeded 40 dBZ within the meso-convective precipitation band and were confined to low levels (below 3 km). The maximum total heat flux (sensible plus latent) from the sea surface into the atmosphere was 1000 W m^{-2}, comparable with that observed for mature tropical cyclones. Satellite cloud images revealed that this polar low was the most intense development in a family outbreak of 5 polar lows that formed as an east-west vortex chain between Iceland and the north coast of Norway over a 48 h period.

1. Introduction

On a historical note, it is only recently that the mesoscale cyclones that form within or at the leading edge of polar air streams have become a focus of research meteorologists (Harley, 1960; Harrold and Browning, 1969; Mansfield, 1974; Rabbe, 1975; Duncan, 1977, 1978; Rassmusen, 1979, 1981, 1983, 1985). These storms, referred to as polar lows, are typically < 500 km in diameter and on occasion contain surface wind speeds above 30 m s^{-1}. The current research interest in polar lows was stimulated by the intriguing satellite cloud images of "hurricane-like," mesoscale, spiral cloud systems, some with cloud-free inner eyes of 20–100 km diameter, that form over the North Atlantic and North Pacific Oceans and their adjacent Arctic seas. Before the advent of meteorological satellites, weather forecasters and researchers relied upon sparse observations from ships and islands, which rarely identified the position, motion, and intensity of polar lows. Norwegian and Icelandic history is filled with tragic accounts of coastal fishermen who ventured out in small open boats, only to be struck and sometimes lost at sea in these violent and unexpected storms. During the early 1940's, the reconnaissance aircraft of the German Luftwaffe and British Royal Air Force were the first to take extensive airborne meteorological observations over the North Atlantic Ocean, the Norwegian and Barents seas, and the adjacent Arctic ice cap (see Schwerdtfeger and Selinger, 1982; Selenger and Glen, 1983). Unfortunately, these wartime observations were not exploited for their scientific content.

In spite of the sparsity of observations, researchers have formulated theories that describe the physical processes governing polar-low development. Mansfield (1974) proposed that polar

lows were the result of baroclinic instability within weakly stratified, shallow (~2 km) marine boundary layers. The small horizontal scale of the lows was attributed to the shallow depth and weak thermal stratification of the baroclinic layer. Reed (1979) and Mullen (1979) noted the importance of tropospheric baroclinity in deep layers (~5 km) on the cyclonic shear side of upper-level jet streams, and suggested that baroclinic instability within deep layers contributed in the initiation of Pacific polar lows and comma clouds.

In contrast to the baroclinic instability proponents, Rasmussen (1979), proposed that polar lows were initiated by cumulus convection through Conditional Instability of the Second Kind (CISK, see Charney and Eliassen, 1964), a mechanism through which latent heating by organized cumulus convection embedded within cyclonic flow initiates vortex spin up, and the resulting enhanced boundary-layer moisture convergence of the vortex feeds and maintains the cumulus elements; this is a positive feedback between the cloud-scale and polar vortex motions. The CISK contribution to polar-low development is a function of both the degree of convective activity and the vertical profile of the latent heating (see e.g., Bratseth, 1985). The lower the altitude of maximum latent heat release, the more rapid and intense the development.

Rasmussen (1985) and Businger (1985) adopted the upper-level baroclinic triggering mechanism of Reed (1979) and Mullen (1979), showing examples where polar low developments were tied to baroclinic waves near the tropopause. The CISK mechanism was relegated to the rapid, deepening phase of the polar low, rather than its initiation. Numerical studies with limited-area mesoscale prediction models have shown the importance of both baroclinic and diabatic processes in the development of polar lows (e.g., Sardie and Warner, 1983).

It is important to note that there are few if any quantitative documentations by weather radar of the intensity and vertical structure of the cumulonimbus convection within polar lows, in contrast to the numerous documentations of deep cumulus convection within tropical cyclones and extratropical continental cyclones. This lack of observational documentation has contributed to the present differences of interpretation regarding the relative contribution by baroclinic processes (baroclinic instability) versus diabatic processes (latent heating within deep cumulus convection), in the life cycle of polar lows.

The present study attempts to fill some of the observational gaps in the understanding of polar low structure through the analysis of the research aircraft, satellite, and synoptic observations of the polar low that formed 200 km south of Jan Mayen on 27 February 1984. These observations were taken during the Arctic Cyclone Expedition, 1984; a collaborative effort between the National Oceanic and Atmospheric Administration (NOAA), the National Aeronautical and Space Administration (NASA), Iceland, Norway, the U.S. Navy and U.S. university researchers. Fig. 1 shows the regional geography for the Arctic Cyclone Expedition.

2. A synoptic-scale perspective: 26–27 February 1984

The evolution of the synoptic-scale (>1000 km) weather systems associated with the polar-low development of 27 February 1984 was captured in the operational analyses of the European Center for Medium Range Weather Forecasts (ECMWF). Our discussion focuses on the 500 mb height and temperature fields, 700 mb height and vertical velocity fields, 1000 mb height and temperature fields, and the temporal changes in the 1000 to 500 mb lapse rate.

Fig. 2 presents the 12-hourly 500 mb height and temperature analyses from 00.00 GMT 26 February through 12.00 GMT 27 February 1984. At 00.00 GMT 26 February (Fig. 2a) a cold-core polar vortex was centered over central Greenland contained core temperatures below −45°C. Southwesterly flow prevailed over the Norwegian Sea from Iceland to the northern coast of Norway. This vortex remained stationary over Greenland during the period of interest. By 12.00 GMT 26 February (Fig. 2b) a synoptic-scale short wave had moved out from the Greenland vortex into the Denmark Strait (the gap between east Greenland and western Iceland). The 500 mb temperatures over the Denmark Strait lowered by ~5°C from those 12 h earlier, and a distinct northwest to southeast thermal trough was

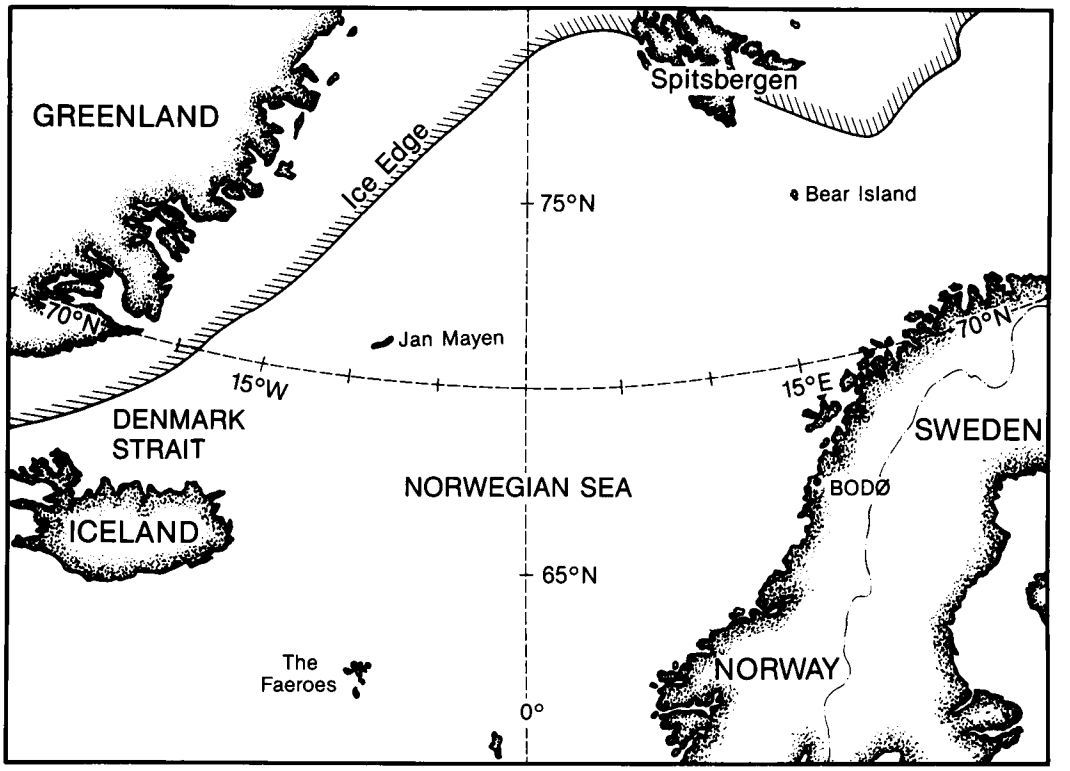

Fig. 1. Regional geography for the Arctic Cyclone Expedition.

located over Iceland in association with the eastward propagating short wave in height field. By 00.00 GMT 27 February (Fig. 2c), the short wave and thermal trough passed east of 10°W and the 500 mb temperatures off the northeast coast of Iceland had lowered by 10°C from those 24 h earlier. It was shortly thereafter that the infrared cloud images from the NOAA-7 and -8 satellites (discussed in Section 7) showed the development of cumulonimbus cloud clusters in the southwesterly flow in advance of the short wave trough axis, the same region within which the polar low was to develop. At 12.00 GMT 27 February (Fig. 2d) the short wave continued eastward across the Norwegian Sea to midway between Iceland and Norway. The low 500 mb temperatures (~ -40°C) had spread east of 10°W, and a band of strong baroclinity extended west to east from the southern tip of Greenland to the northern coast of Norway.

The 700 mb vertical velocity fields (Fig. 3) documented the vertical velocities associated with the propagating short wave. At 12.00 GMT 26 February, the 700 mb vertical velocity field showed the characteristic dipole for a short wave, then centered over the Denmark Strait; with ascent ahead and descent behind of the wave trough axis. The vertical velocity dipole moved eastward with the short wave during the following 24 h, such that by 12.00 GMT 27 February (the time of initial polar low penetration by the NOAA research aircraft) the ascent in advance of the short wave trough had reached the eastern Norwegian Sea.

The 1000 mb height analysis at 12.00 GMT 26 February (Fig. 4a) contained a -40 m low center in the eastern lee of Greenland. The companion surface temperature field contained strong low-level baroclinity, which extended parallel to the east-Greenland ice edge, from the southern tip of Greenland northeastward to Spitsbergen. At this time, the surface low, which had been stationary for the previous 24 h, began its eastward movement into the Norwegian Sea, in response to the

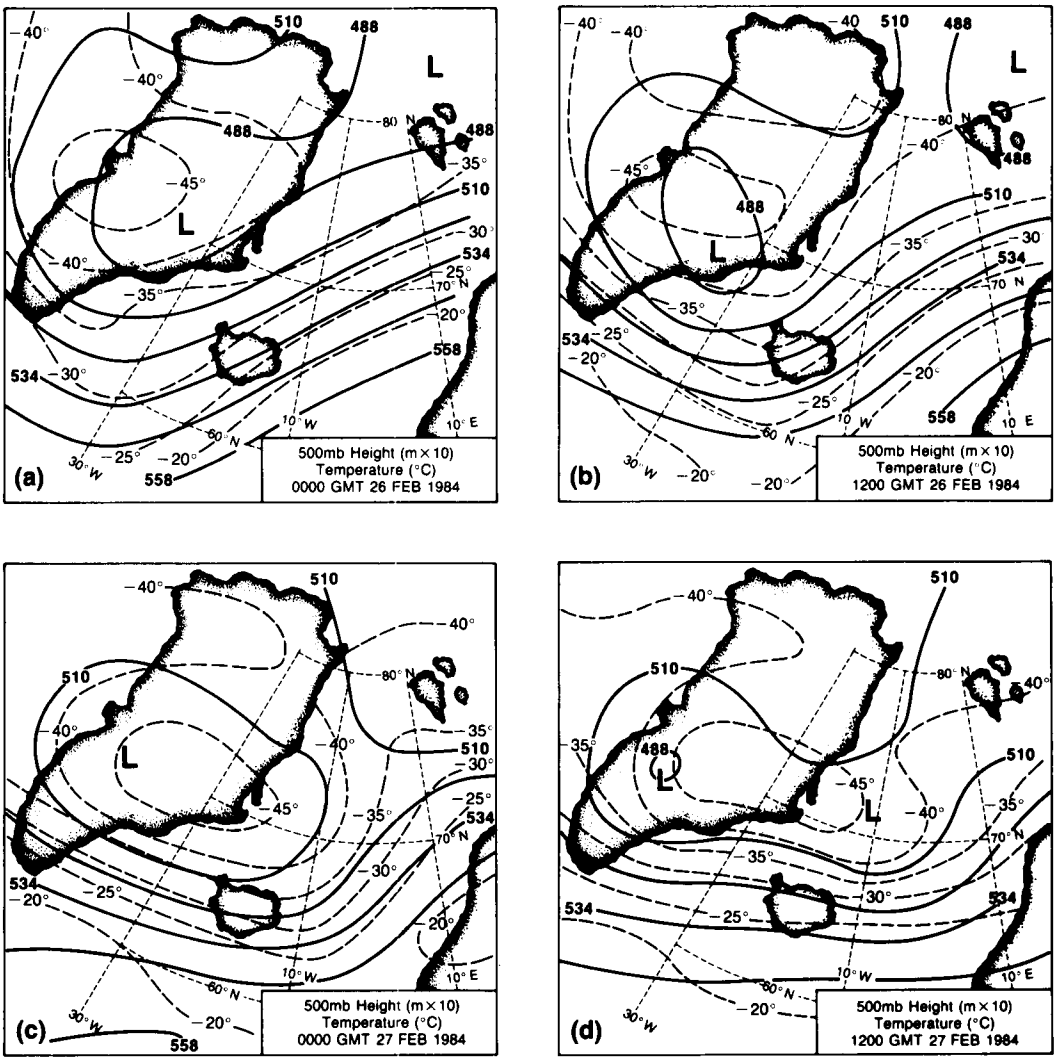

Fig. 2. The 500 mb height (×10 m, solid lines) and temperature (°C, dashed lines) from the ECMWF analysis. (a) 00.00 GMT 26 February 1984, (b) 12.00 GMT 26 February 1984, (c) 00.00 GMT 27 February 1984, (d) 12.00 GMT 27 February 1984.

synoptically forced vertical circulation of the propagating upper-level short wave (Figs. 2, 3). By 12.00 GMT 27 February (Fig. 4b), the surface low had travelled into the eastern Norwegian Sea in advance of the short wave aloft, with little change in intensity, and an intense polar was spawned at the circled cross mark in the southwestern sector of the synoptic-scale cyclone.

It is instructive to view the ECMWF temperature lapse rates over the region of polar low development for the period 26 through 27 February 1984. Fig. 5 presents the 12-hourly temperature profiles at the crossmark of Fig. 4b. At 00.00 GMT 26 February, the lapse rate was stable to moist adiabatic ascent. As the cold air within the upper-level short wave, moved out over the Norwegian Sea (Fig. 2), the upper troposphere cooled at a more rapid rate than the near-surface and lower-tropospheric air over the region of polar low development. At the time of

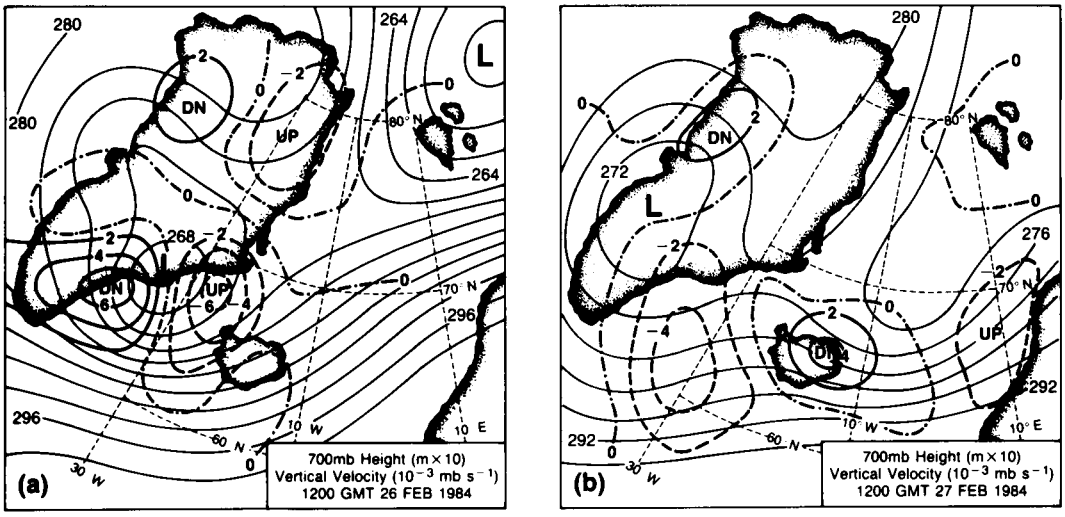

Fig. 3. The 700 mb heights (×10 m, thin lines) and vertical velocity (10^{-3} mb s^{-1}; positive, heavy solid lines; negative, heavy dashed lines; zero isopleth, dashed and dotted line) from the ECMWF analysis. (a) 12.00 GMT 26 February 1984, (b) 12.00 GMT 27 February 1984.

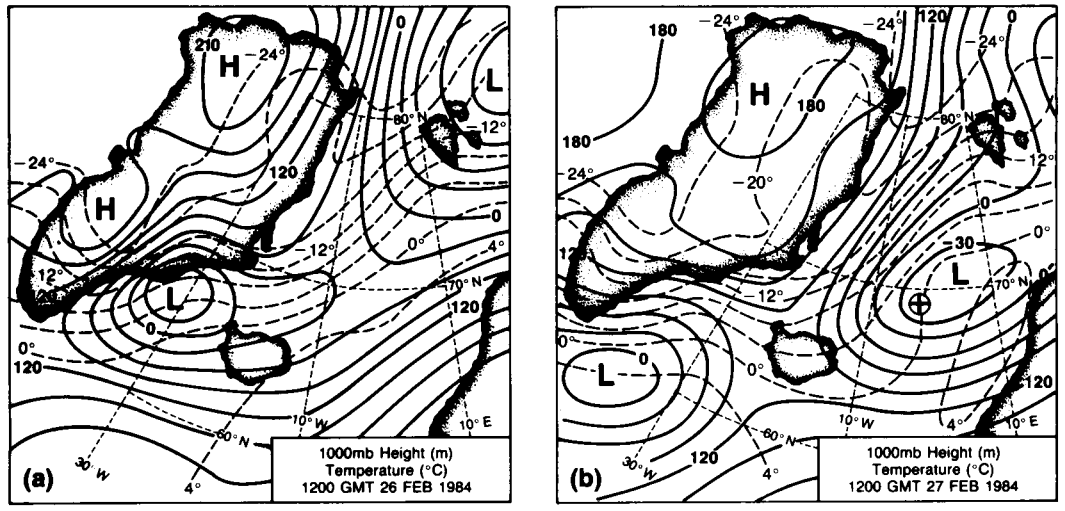

Fig. 4. The 1000 mb height (×m, solid lines) and temperature (°C, dashed lines) from the ECMWF analysis. (a) 12.00 GMT 26 February 1984, (b) 12.00 GMT 27 February 1984 (the circled cross mark is the position of the polar low featured in Fig. 9).

the maximum intensity of the polar low (~12.00 GMT 27 February), the lapse rate exceeded the moist adiabat (conditionally unstable) in the 1000 to 700 mb layer (Fig. 5). The 500 mb temperature lowered by 13°C over the 36 h period as compared with the lesser 5°C cooling of the air near the sea surface in the region of polar-low development. The destabilization of the temperature lapse rate was also due, in part, to the sensible heating of the boundary-layer air by the underlying ocean surface. The cold-air advection associated with the surface flow from off the Greenland ice edge into the Norwegian Sea was partially compensated by the upward sensible

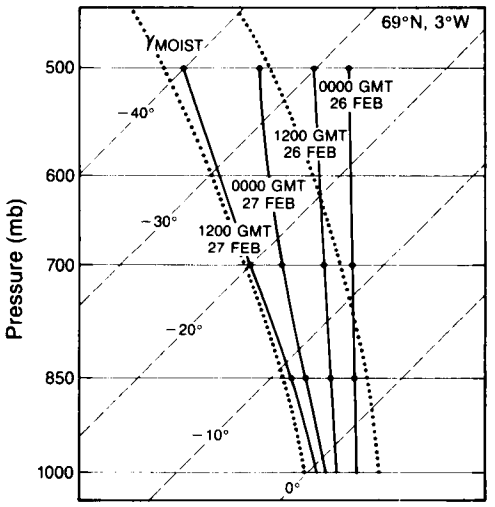

Fig. 5. Temperature profiles (heavy solid lines) over the region of polar low development (at 69°N, 3°W, the cross mark of Fig. 4) for the period 00.00 GMT 26 February through 12.00 GMT 27 February 1984 from the ECMWF analysis. Moist adiabats, dotted lines; isotherms (°C, dashed lines).

heat flux from the warmer underlying ocean surface (see Section 6).

In summary, the ECMWF synoptic perspective clearly shows that synoptic-scale upper-level baroclinic forcing was present in the region of polar low spin up. The polar low described in this study developed in the area of synoptic-scale upward vertical motion in advance of an eastward-propagating upper-level short wave trough axis, and at the leading edge of the Arctic cold-air outbreak. The synoptic ambient temperature lapse rate became conditionally unstable during the period of polar low development, a favorable condition for the development of cumulonimbus clouds within the polar low.

3. Instrumentation and data sources

The NOAA WP-3D (P-3) research aircraft measured and recorded standard navigational and meteorological parameters. Omega-navigation dropwindsondes were released to obtain vertical profiles of wind, temperature, and moisture. An airborne downward-looking infrared radiometer remotely sensed sea-surface temperatures. Airborne lower-fuselage and tail-mounted radars provided reflectivity and Doppler motions of the precipitation elements within the storm. The polar-orbiting NOAA-7 and -8, Defense Meteorological Satellite Program (DMSP), and METEOSAT satellites provided cloud and sea-ice infrared imagery. Satellite observations of total columnar ozone were measured with the Total Ozone Mapping Spectrometer (TOMS). Synoptic surface and upper-air observations were integrated with the NOAA aircraft mesoscale observations.

4. The flight into the polar low of 27 February 1984

In the pre-dawn hours of 27 February 1984, the NOAA flight engineers prepared the aircraft for an 08.00 GMT departure from Bodo, Norway, as the expedition scientists and the Norwegian Meteorological Institute (DNMI) meteorologists discussed their diagnosis of the synoptic reports and numerical forecasts. Since real-time satellite images were not available in Bodo, the DNMI meteorologists in Oslo, Norway telephoned their interpretation of the NOAA-7 and -8 images to the expedition. Their interpretation was of off-ice flow west of Spitsbergen and the possibility of polar-low development south of Jan Mayen. The surface analyses at 12.00 GMT 26 February (Fig. 4a) and 00.00 GMT 27 February 1984 showed strong northerly flow west of Spitsbergen. After a very lively discussion between the expedition scientists, the decision was made to fly north toward Spitsbergen for further studies of boundary-layer processes and ice-edge frontogenesis. The developing cumulonimbus cloud clusters south of Jan Mayen did not possess sufficient polar-low qualities to warrant their investigation.

The NOAA aircraft departed Bodo, Norway, at 08.10 GMT and headed northward toward Spitsbergen and its adjacent ice edge at a flight altitude of 3.6 km. Fig. 6 shows the aircraft flight track, schematic renderings of key cloud features from the 13.40 GMT NOAA-7 satellite infrared imagery, upper-level (flight level) winds, and the positions of the dropwindsonde deployments. The first dropwindsonde was deployed at 09.00 GMT (500 km north of Bodo) as the aircraft approached a frontal cloud band. The aircraft then descended to 300 m and took measurements

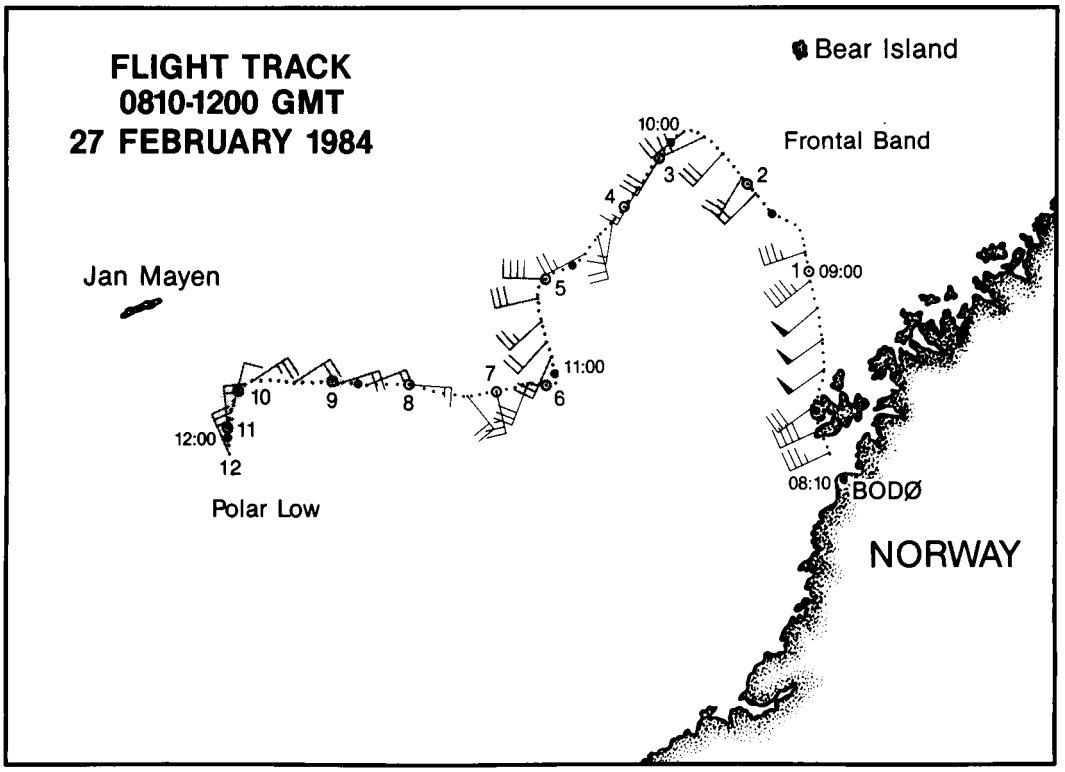

Fig. 6. NOAA aircraft flight track (dotted line) at 3.6 to 4.2 km altitude between 08.10 and 12.00 GMT 27 February 1984. Wind vectors are flight-level winds: flag = 25 m s^{-1}, full barb = 5 m s^{-1}, and half barb = 2.5 m s^{-1}. Half-hour time hacks indicated by solid circles with hourly time (GMT). Positions of dropwindsonde deployments are indicated and numbered at open, center-dotted circles. Cloud silhouettes of the frontal band and the polar low from the 13.40 GMT 27 February 1984 NOAA satellite infrared image (Fig. 28a), stippled areas.

of the front. The front was poorly defined, so the aircraft climbed to 4.2 km, deployed the second dropwindsonde, and proceeded northward toward Spitsbergen.

At 09.45 GMT, a radio message was received from Bodo "Intense cyclonic cloud system ... looks interesting ... 69°N 3° ...." The Oslo meteorologists had reviewed the 08.25 GMT satellite image, and telephoned their interpretation to the Bodo weather office, who in turn transferred the message to the Bodo Air Traffic Control (ATC) center for radio transmission to the NOAA aircraft. The reception of the radio transmission terminated short of its completion. It was not known whether the cloud system was at 3°E or 3°W. Repeated attempts to contact the Bodo ATC were without success. A quick decision was vital, since the aircraft was flying in the opposite direction of the sighted cyclonic cloud system. Twenty minutes later, the radio silence was broken, "Polar low south of Jan Mayen". At 10.00 GMT, the aircraft turned southwestward in pursuit of the storm.

Because of the uncertainty in the position of the polar low, the flight-level winds, dropwindsonde profiles, and cloud structure as viewed from the aircraft, were used to search for the storm. The aircraft proceeded southwestward at 580 mb (4.2 km) toward 69°N 3°W, deploying dropwindsondes 3 and 4 (Fig. 6) at 10.04 and 10.13 GMT, both of which failed to provide wind profiles. As the aircraft exited the cirrus shield of the frontal cloud band, a second cirrus shield appeared ahead, and the aircraft passed beneath its leading edge and deployed dropwindsonde 5 (Fig. 6) at 10.35 GMT. This second cloud shield was interpreted as the ~7 km outflow from cumulonimbus clouds within the polar low. At

10.40 GMT, the aircraft turned due south under the shield toward 69°N. As the aircraft passed beneath the cirrus, the sun remained visible on the southern horizon, and the boundary-layer cumulus clouds were topped off at ~2 km. There were no cumulonimbus towers connecting the moist boundary layer with the high-level cirrus shield in the direction that the aircraft was flying. At 11.00 GMT, the aircraft reached the southern edge of the cirrus shield, released dropwindsonde 6 and turned westward. As the aircraft proceeded westward, the flight-level winds turned from southwesterly to southerly and then easterly. The sea-surface wind reports from dropwindsondes 5 and 6 (Fig. 6) were 5 m s^{-1}, northeasterly and 10 m s^{-1}, southeasterly, respectively, indicating weak cyclonic flow below. However by the time these reports were available, the aircraft had already reached the point midway between dropwindsondes 8 and 9 (Fig. 6). At 11.50 GMT the aircraft was surrounded by cumulonimbus towers that reached from the boundary layer to the cirrus shield at ~7 km. The low-level winds from dropwindsondes 8 and 9 were ~5 m s^{-1}, southwesterly and northeasterly, respectively; there was no indication of strong low-level winds characteristic of a mature polar low. By 11.50 GMT, the flight-level winds had turned northeasterly, suggesting that a cyclonic circulation was located southwest of the aircraft's present position. Dropwindsonde 10 was deployed (and failed) as the aircraft turned southward toward 69°N, 3°W.

At this point in the search, one half of the mission flight hours had been expended, the aircraft was enveloped in thick cloud, and the dropwindsondes gave no evidence for strong surface winds. It was decided to descend to 300 m to search for the polar low circulation. Dropwindsonde 11 was released at 12.00 GMT, and at 12.05 GMT the aircraft began a slow (300 m min^{-1}) descent toward the sea and released dropwindsonde 12. As dropwindsonde 11 passed through the 2 km level, its telemetered winds increased to above 25 m s^{-1}, and by 150 m, exceeded 30 m s^{-1}, with a direction of due north. We had located the strong low-level winds associated with the polar low. The aircraft continued its descent in heavy turbulence within the cumulonimbus clouds of the polar low. Fig. 7 shows the profiles of wind velocity, potential temperature, and moisture mixing ratio during

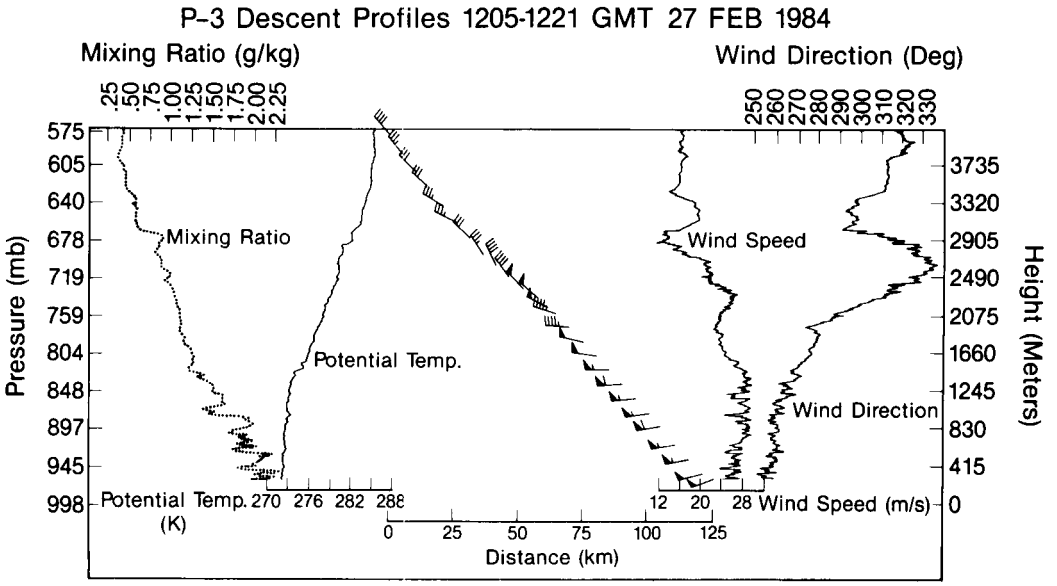

Fig. 7. NOAA aircraft descent profiles of water-vapor mixing ratio (g kg^{-1}), potential temperature (K), wind vectors as a function of distance on a flight track heading of 180°, wind speed (m s^{-1}), and wind direction (deg) between 12.05 to 12.21 GMT 27 February 1984. Flags and barbs are the same as in Fig. 6.

the descent. The aircraft broke out of the clouds at 500 m into 27 m s^{-1} southwesterly winds and proceeded down to 300 m above the wind-driven 8-m-high sea swells and ocean foam streaks. The remainder of the flight documented the wind, temperature, moisture, and precipitation distribution about the polar low.

5. The structure of the polar low of 27 February 1984

The structure of the 27 February 1984 polar low was derived from the composite analysis of NOAA aircraft flight-level observations, dropwindsonde profiles, precipitation observations with airborne radar, sea-surface temperatures from the downward-looking infrared radiometer, and pressure-height observations from an airborne radar altimeter. The observations were space-time adjusted (Taylor hypothesis) to 13.40 GMT 27 February 1984, the time of the first aircraft low-level penetration of the storm center. The phase velocity for this adjustment was 13 m s^{-1} toward the east-southeast (113°), determined from the polar-low cloud vortex motion in the satellite images.

Fig. 8 shows the 300 m space-time adjusted flight track with time hacks (GMT), flight-level wind vectors, cross section projection line AA′ used in analyzing the vertical structure (Section 5.2), and the underlay of the 300 m streamlines (from Fig. 10a). The short southwestward flight track beginning at 12.21 GMT was from the measurements taken immediately after the descent profile (Fig. 7). From 12.24 GMT to 13.15 GMT, the aircraft took Doppler radar observations at 1.7 km (~830 mb) in the area

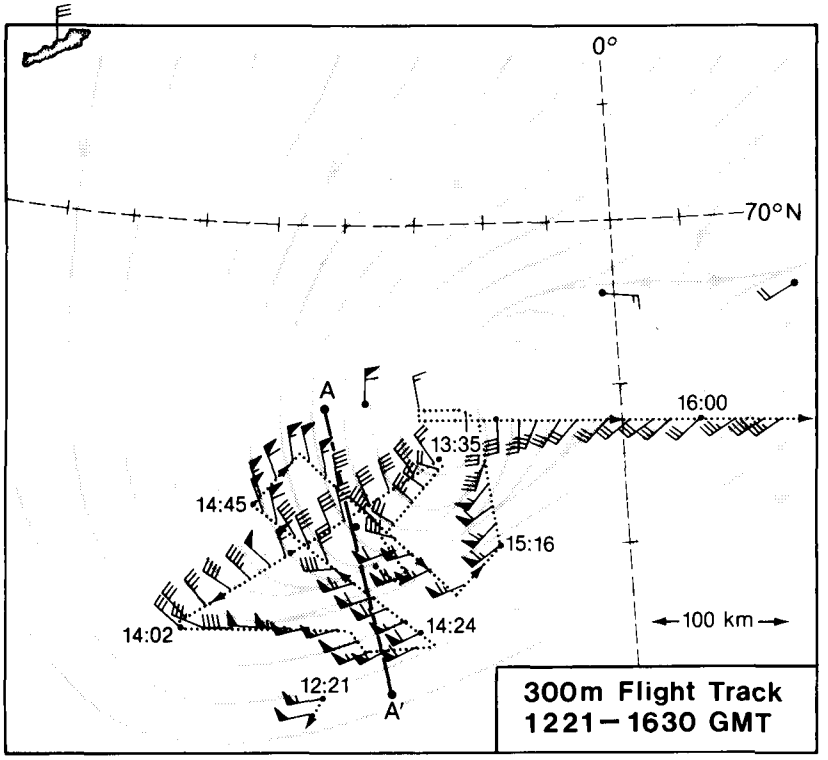

Fig. 8. NOAA aircraft 300 m flight track between 12.21 and 16.10 GMT 27 February 1984. Wind vectors along dotted flight track are 300 m flight-level winds. Dropwindsonde wind vectors at or below 300 m have heavy dotted heads. Line AA′ is the cross-section projection line for Figs. 19–23. Flags and barbs are the same as in Fig. 6. Streamlines of the 300 m wind from Fig. 10a are the gray-shaded lines.

west of line AA′ (Fig. 8). Observations from the dropwindsondes, the 12.00 GMT rawinsondes from Jan Mayen and a Soviet ship east of Iceland, and regional analyses from conventional data sets were composited with the NOAA aircraft measurements.

5.1. Horizontal structure

The surface pressure analysis (Fig. 9) was prepared from observations from Jan Mayen, the surface pressure estimates from the dropwindsondes, and the 300 m aircraft radar altimeter observations. The analysis shows the 979 mb low-pressure center at 69°N, 3°W. The lowest pressure was measured at the point of calm winds, encountered at ~16.00 GMT (Fig. 8) during the final penetration of the polar low. The mean radial pressure gradient from the storm center out to a radius of 200 km was 17 mb (200 km)$^{-1}$. This corresponded to a mean geostrophic tangential speed of ~45 m s^{-1}, which because of the cyclonic flow was more than twice the ~20 m s^{-1} mean observed tangential wind speed within the 200 km radius. Reference to Fig. 4b provides the synoptic-scale surface pressure field within which the meso-α-scale (~400 km) polar low of Fig. 9 was situated.

The 300 m wind velocity analysis is presented in the streamlines and isotachs of Fig. 10. The streamlines (Fig. 10a) show the center of the polar low at ~69°N, 3°W. The 300 m flow contained a prominent confluent asymptote between the north to northwesterly flow from off the Greenland ice edge and the west to southwesterly flow from off of Iceland. This asymptote was crossed four times during the aircraft mapping of the 300 m structure. The asymptote was strongly convergent and baroclinic, and contained the heaviest precipitation encountered during the interrogation of the storm, but not necessarily the most intense precipitation during its life cycle. A second con-

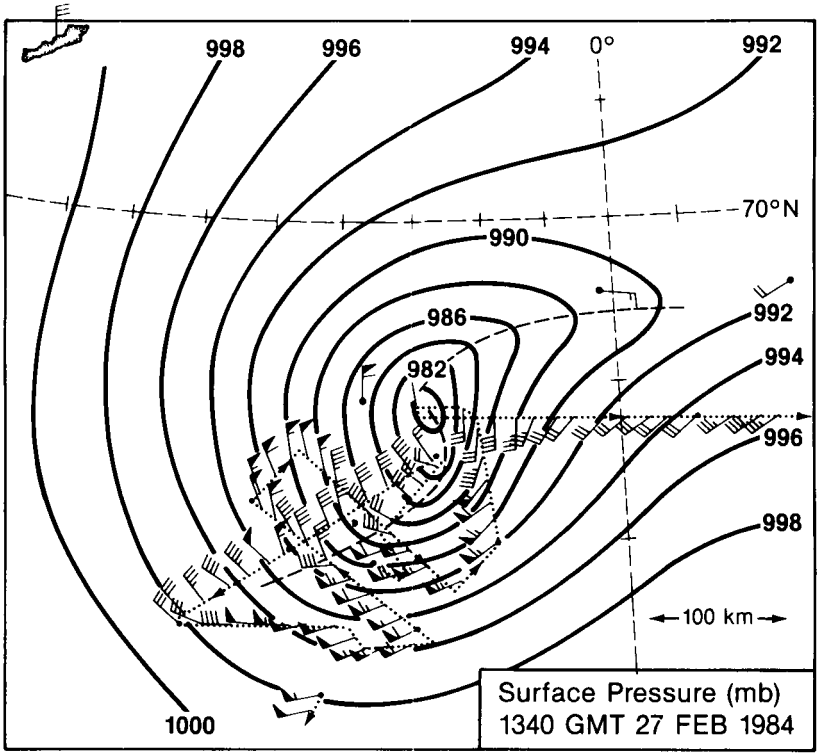

Fig. 9. The surface pressure analysis (mb) at 13.40 GMT 27 February 1984. Flight track and wind vectors are the same as shown in Fig. 8.

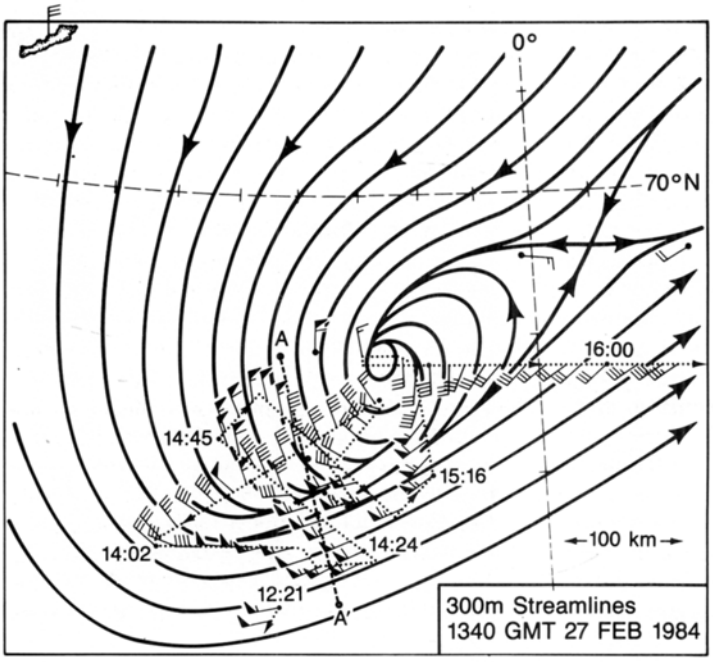

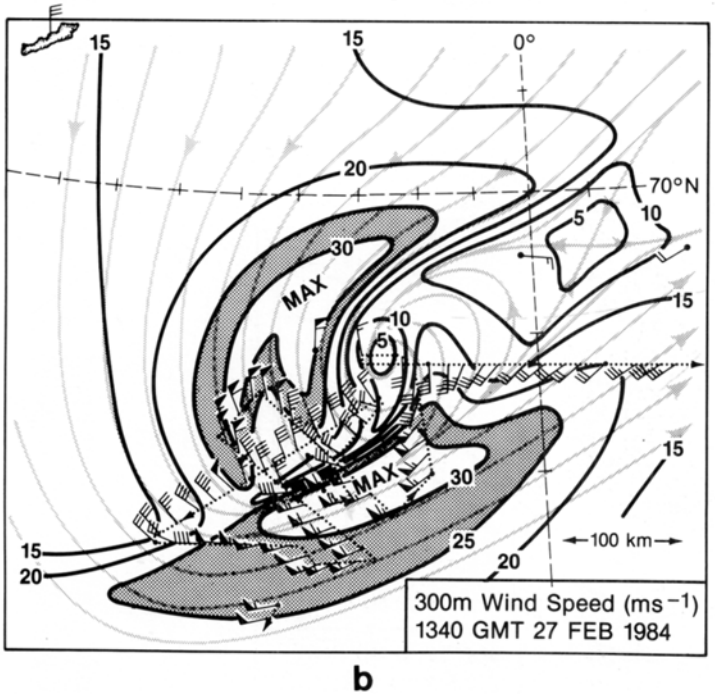

Fig. 10. The 300 m wind velocity analysis at 13.40 GMT 27 February 1984. (a) streamlines and (b) wind speed isotachs (m s^{-1}, solid lines). Gray-shaded streamlines in Fig. 10b are from Fig. 10a. Flight tracks and wind vectors are the same as shown in Fig. 8.

fluent asymptote spiraled in toward the low center from the northeast, but was not well documented by the aircraft or dropwindsonde measurements. Southeast to east of the low center, a diffluent asymptote extended northeastward toward a col-point singularity at 69.5°N, 1°E. The col separated the mature polar low from a developing polar low to the northeast. The streamlines of the 300 m flow field contained considerable asymmetry about the low center. The inflow into the polar low was concentrated within the two primary confluent asymptotes.

The 300 m wind-speed analysis (Fig. 10b) contains two speed maxima exceeding 30 m s^{-1}, one in the northerly flow north of the prominent confluent asymptote of Fig. 10a, and the second in the southwesterly flow in advance of the asymptote. The speed maxima were situated ~100 km from the low center, and narrow bands of large cyclonic speed shear were found at their flanks. One zone of low wind speed extended southwestward from the low center along the narow zone of maximum cyclonic curvature north of the southern confluent asymptote, and a second bridged the two areas of calm winds between the storm center and the col point to its northeast. Just as with the streamline field, the wind speeds were asymmetrically distributed about the polar low.

The 300 m relative vorticity analysis (Fig. 11) shows two bands of high vorticity that extended outward from the low center, with maximum values exceeding 20×10^{-4} s^{-1}. The southwestern vorticity band was the combination of cyclonic curvature north of the southern confluent asymptote (Fig. 10a) and the cyclonic shear on the northern flank of the southwesterly wind speed maxima (Fig. 10b). The northern vorticity band reflected the cyclonic speed shear on the eastern flank of the northern wind speed maximum (Fig. 10b). The dimensions and magnitude of this "serpentine" shaped vorticity maximum were

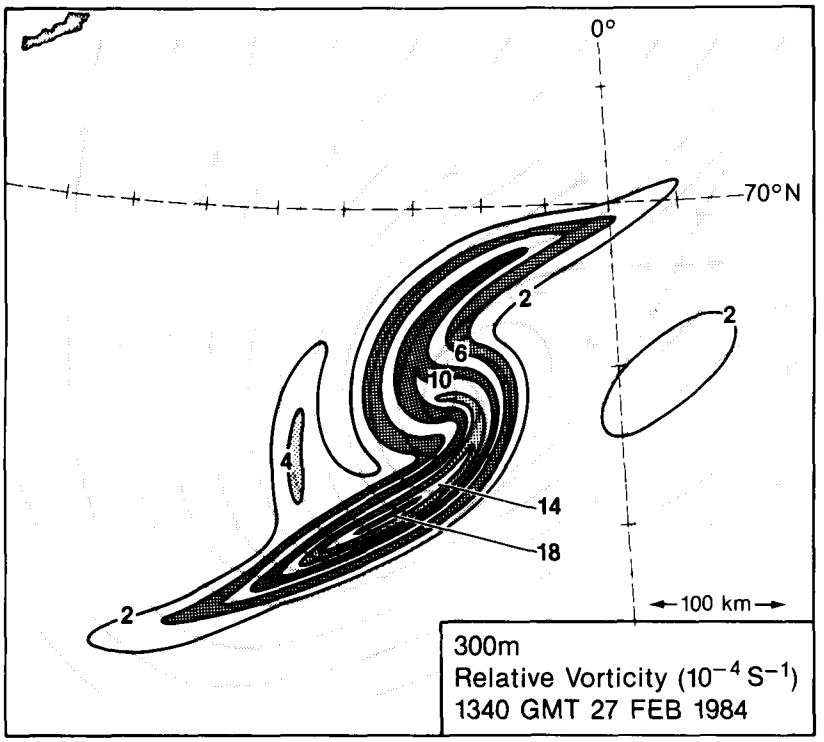

Fig. 11. Relative vorticity of the 300 m wind ($\times 10^{-4}$ s^{-1}, solid lines) at 13.40 GMT 27 February 1984. Gray-shaded streamlines are from Fig. 10a.

mesoscale, being ~400 km in length, ~50–100 km in width, and more than 1 order of magnitude larger than the Coriolis parameter.

The 300 m temperature analysis (Fig. 12) was derived from a composite of 300 m flight-level temperatures, dropwindsonde temperatures, and the Jan Mayen 300 m radiosonde temperature. A tongue of warm temperatures, warmer than −3°C, extended northeast to southwest into the cyclonic circulation of the low. The highest temperatures of ~ −0.5°C were found within the warm pool 100 km southwest of the low center. Lower temperatures of −8.5°C and −5°C were found northwest and south of the low center, respectively. The 300 m thermal field had the appearance of the final phase of a mesoscale occlusion, as the cold air entrapped (secluded) a mass of warmer air near the center of the polar low. The process of cold air intruding and cyclonically wrapping itself about a relatively warmer air mass, thereby isolating it from its parent warm air source, was termed a "seclusion" by Bergeron (1928). In this case, we suggest that the warm core seclusion was the final phase in the baroclinic evolution of this polar low. Another significant thermal feature was the narrow zone of meso-β-scale (~10 km) thermal gradient coincident with the southern confluent asymptote (Fig. 10a). Though not a front in the classical sense, we shall hereafter refer to this mesoscale baroclinic zone as a front for the purpose of simplicity of discussion. The front was penetrated by the aircraft twice during the 300 m horizontal intercepts of the asymptote. The vertical structure of this front is described in Subsection 5.2.

A synoptic view of the lower-tropospheric thermal structure of the polar low environment is shown in the 850 mb temperature analysis (Fig. 13), prepared from the 12.00 GMT 27 February 1984 land and ship rawinsonde soundings, NOAA aircraft ~850 mb flight-level data, and

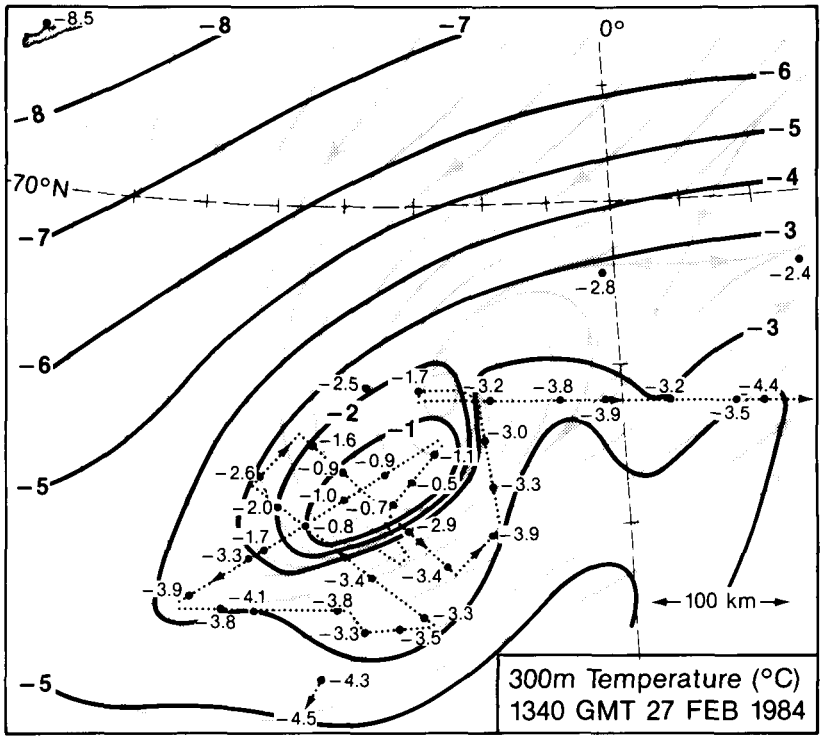

Fig. 12. The 300 m temperature analysis (°C) at 13.40 GMT 27 February 1984. Selected temperatures (°C) are plotted along the aircraft flight track, at dropwindsonde positions, and at Jan Mayen. Gray-shaded streamlines are from Fig. 10a.

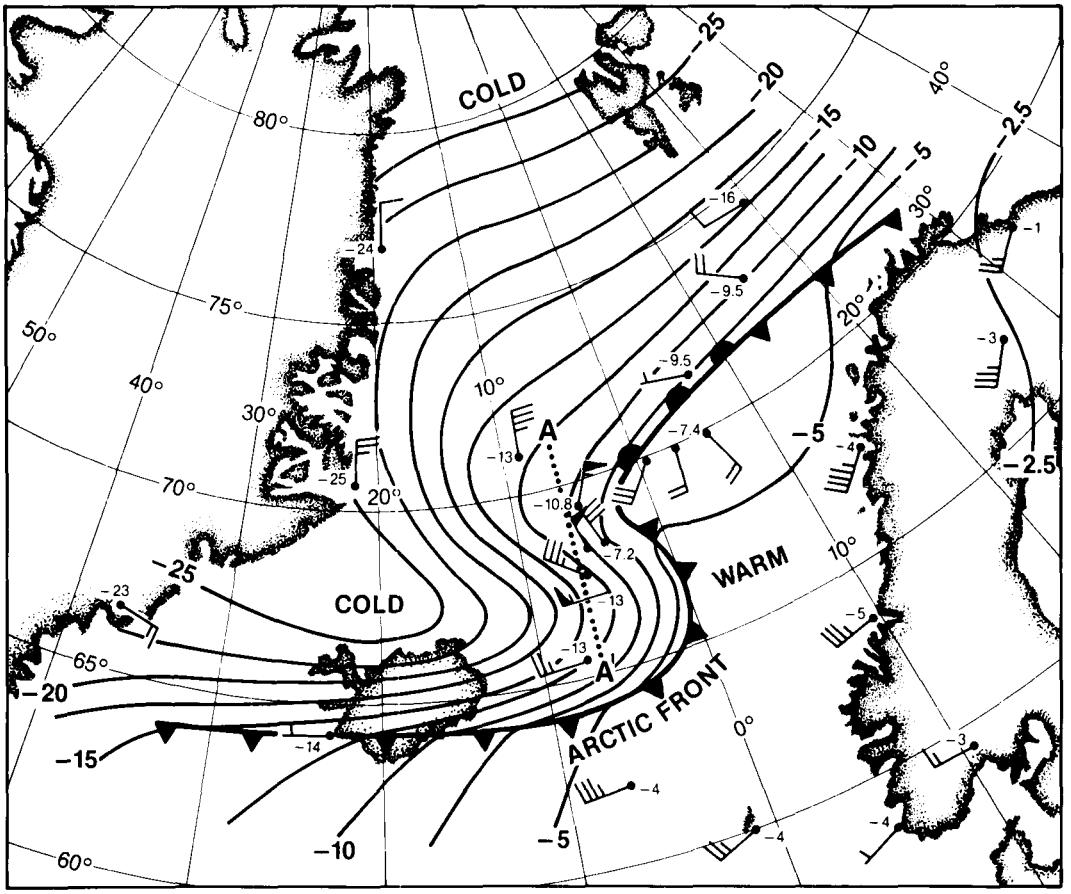

850mb TEMPERATURE (°C) 1200 GMT 27 FEBRUARY 1984

Fig. 13. The 850 mb temperature analysis (°C) at 12.00 GMT 27 February 1984, prepared from conventional rawinsonde observations, NOAA aircraft ~850 mb flight-level measurements, and aircraft dropwindsonde data. Selected 850 mb temperatures (°C) are plotted next to 850 mb wind vectors. Wind vector flags and barbs are the same as in Fig. 6. The leading edge of the Arctic front is shown by the heavy spiked line. Dotted line AA′ is the cross-section projection line for Fig. 18.

dropwindsonde profiles. The analysis shows that cold, −15°C to −25°C, air was drawn southward along the eastern lee of Greenland. The east coast of Greenland is a 3-km-high barrier, which blocked the westward motion of cold-air outbreak that originated from the polar ice cap to the north. The polar air was channeled southward over the zone of solid sea-ice pack that parallels the Greenland coast (see Fig. 1) without experiencing significant temperature changes. Note the < -20°C 850 mb temperatures along the Greenland coast as far south as 65°N. As the cold, northerly flow approached Iceland, it turned cyclonically eastward toward the northern coast of Norway. The eastward surge of cold air over Iceland was tied to the synoptic-scale cyclonic circulation within the lower troposphere (see also Fig. 4b). The eastward surge of cold air was evident at 300 m in the southwesterly flow south of the polar low (Fig. 12).

The layer-average thermal structure of the polar low was derived from a thickness analysis for the layer 580 to 1013 mb. The 1013 mb heights were obtained from the sea-level pressure analysis (Fig. 9). The 580 mb aircraft altimeter heights were composited with the regional

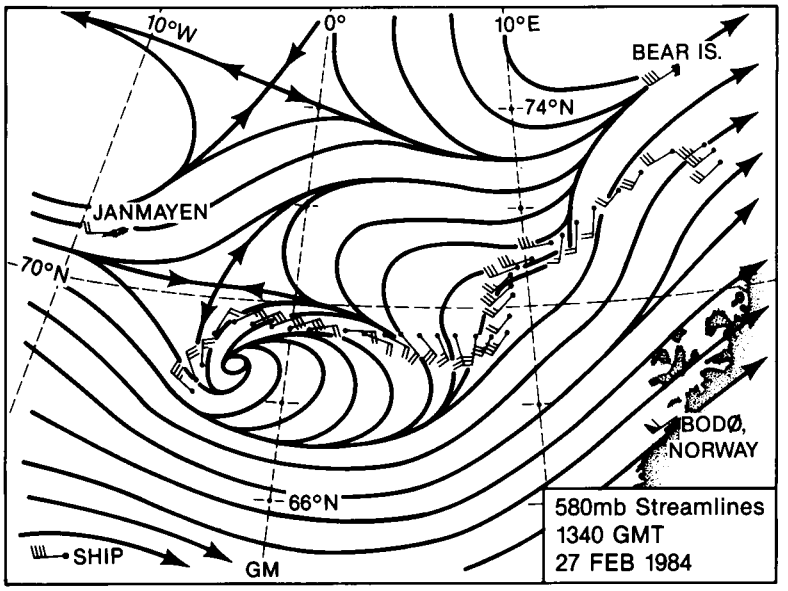

Fig. 14. The 580 mb streamline analysis at 13.40 GMT 27 February 1984. NOAA aircraft flight-level winds are the wind vectors with dotted heads; 12.00 GMT synoptic upper-air winds are the wind vectors without dotted heads. Wind flags and barbs are the same as in Fig. 6.

rawinsonde observations and the 700 and 500 mb ECMWF height analyses to obtain a 580 mb height analysis (not shown) over the polar low. Instead we present the 580 mb streamline analysis (Fig. 14), which shows the <15 m s^{-1} cyclonic circulation at $\sim 69°$ N, 3° W, centered directly above the >30 m s^{-1} wind speeds of the 300 m circulation (Fig. 10) of the polar low. The thickness-temperature analysis (Fig. 15) shows that the polar low had a warm inner core. The central-

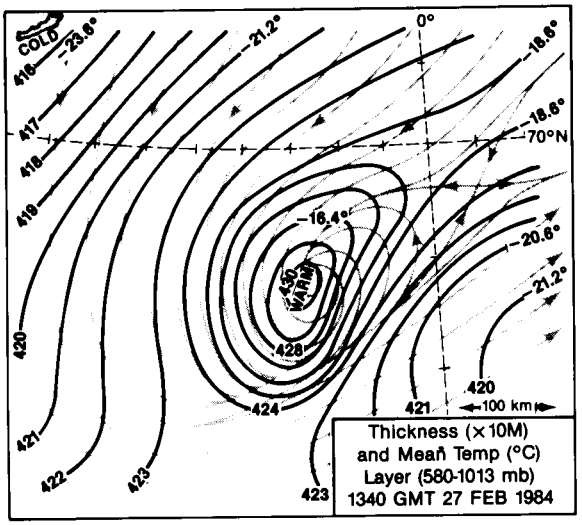

Fig. 15. Thickness (× 10 m) and mean temperature (°C) analysis for the layer 580 to 1013 mb at 13.40 GMT 27 February 1984. Gray-shaded lines are the 300 m streamlines from Fig. 10a.

core temperature of ~ -15°C was 5°C warmer than that at 200 km distance from the center of the low. Thus, both the 300 m and the 580 to 1013 mb thickness temperatures showed that the polar low possessed a warm inner core.

5.2. *Vertical structure*

The vertical structure of the polar low was derived from selected cross-section analyses that incorporated observations from the 12.00 GMT rawinsondes from Jan Mayen and a Soviet ship southeast of Iceland, NOAA aircraft dropwindsondes 11 and 12 (Fig. 6), aircraft descent profiles (Figs. 7, 16), and the 14.26 to 14.40 GMT 300 m aircraft penetration of the low (Fig. 17). The first cross section (Fig. 18) shows the potential temperature along the line AA′ of Fig. 13. The section cuts across the polar low, passing through the pocket of warm 300 m, 850 mb, and 580 to 1013 mb temperatures (Figs. 12, 13, 15, respectively), the confluent asymptote and front southwest of the low center (Figs. 10, 12), and the tongue of cold southwesterly flow south of the low center (Figs. 12, 13). This analysis contains several features of interest. The northerly boundary-layer flow off the Greenland ice edge was capped by a strong inversion centered at 1.25 km (875 mb). The strength of the inversion decreased with increasing distance south of the ice edge. The baroclinity of the neutrally stratified ($\partial\theta/\partial p \approx 0$) boundary layer between Jan Mayen and dropwindsonde 12 reflected the sensible heating of the layer (see Section 6) as the surface air flowed southward off the ~ -20°C ice edge out over the ~ 2°C sea surface. This baroclinity was also evident in the 300 m temperature analysis (Fig. 12). The warm core of the polar low was situated at the region of downward deformation of the warm isentropes at the center of the cross section. The axis of the warm core extended upward from the sea surface at the leading edge of the surface front and sloped southward with increasing height to become continuous with the top of the $\sim$2-km-deep stable layer. This southern stable layer capped a neutrally-stable boundary layer containing the cold surface and 850 mb flow off Iceland that was evident in Figs. 12, 13.

A second cross-section was prepared to illustrate the mesoscale structure of the polar low along the projection line AA′ of Fig. 8. The section cuts through the confluent asymptote and frontal zone of Figs. 10, 12. Data sources for this cross section were the same as for Fig. 18; however, the second cross section treats additional fields, and is more detailed in its depiction of the mesoscale features. Analyses were prepared for potential temperature θ, equivalent potential temperature θ_e, wind components

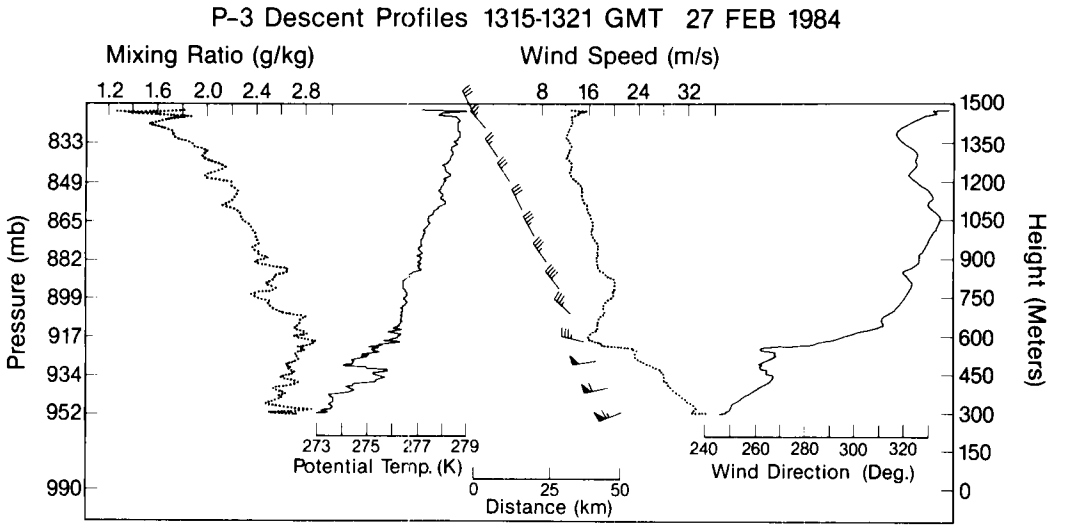

Fig. 16. NOAA aircraft descent profiles for the period 13.15 to 13.21 GMT 27 February 1984. Traces and wind vectors are the same as used in Fig. 7.

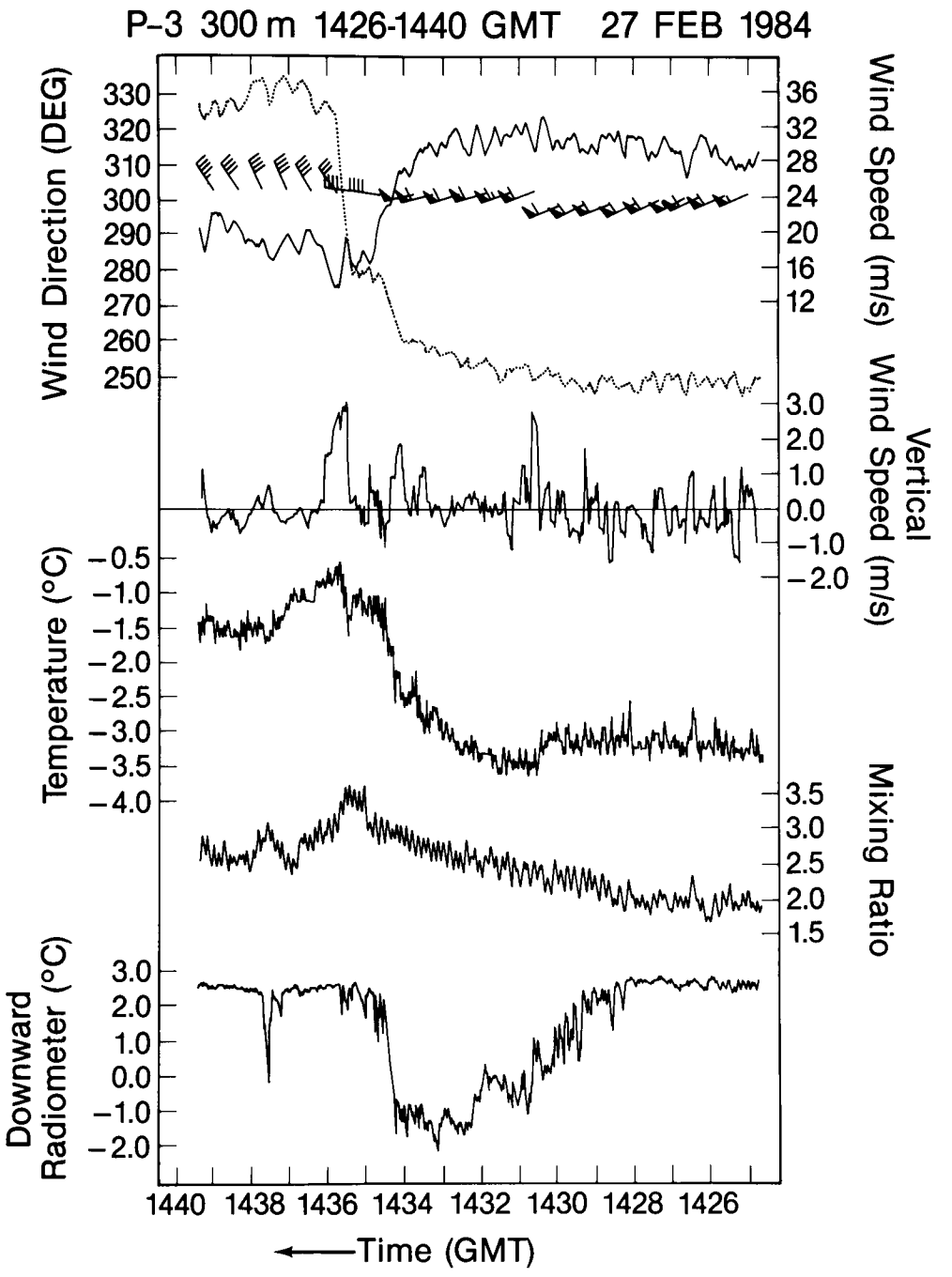

Fig. 17. NOAA aircraft 300 m flight-level traces for the period 14.26 to 14.40 GMT 27 February 1984 of horizontal wind direction (deg), wind speed (m s^{-1}), horizontal wind velocity vectors (as in Fig. 6), vertical velocity (m s^{-1}), temperature (°C), water-vapour mixing ratio (g kg^{-1}), and downward-looking infrared radiometer temperature (°C).

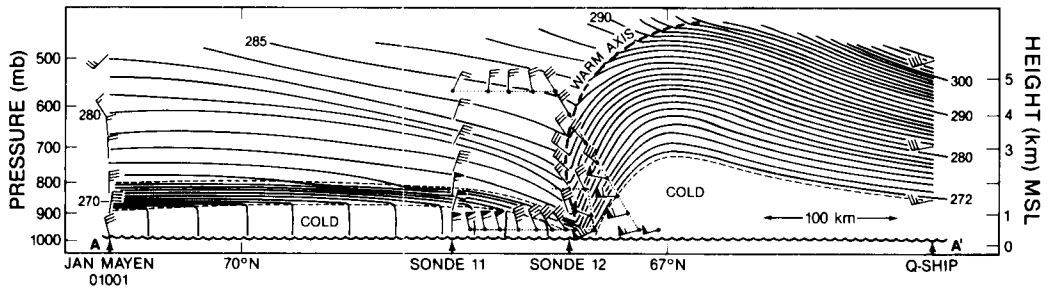

Fig. 18. Cross-section analysis of potential temperature (K, thin solid lines) along the projection line AA′ of Fig. 13 at 13.40 GMT 27 February 1984. Frontal and boundary layer boundaries, thin dashed lines. Warm axis of the polar low and upper boundary of the southern frontal zone, heavy dashed line. NOAA aircraft flight track, dotted line; selected winds, vectors with dotted heads; 12.00 GMT rawinsonde and aircraft dropwindsonde, winds, vectors without dotted heads. Wind flags and barbs are the same as in Fig. 6.

perpendicular and parallel to the cross section (u, v respectively), and absolute momentum m. In addition, calculations were made of vorticity, divergence, vertical motion, and storm-relative vertical circulation.

The cross section of potential temperature and the wind component perpendicular to the projection line AA′ of Fig. 8 is shown in Fig. 19. The potential temperature analysis contains two layers of enhanced thermal stratification that capped the near-neutrally stable marine boundary layer. The stable layer over the north-to-northwesterly boundary layer flow was only ~ 1 km deep and possessed little slope. The stable layer over the west-to-southwesterly boundary-layer flow was ~ 2.5 km deep, and sloped downward to the sea surface, forming a sharp, narrow (~ 10 km) front at the confluence and convergence of the northwesterly and southwesterly flow at the southern asymptote of Fig. 10a. The front broadened to 50 km in width by 1.5 km above the sea, separating the warm core of the polar low from the cold air to the south. The thermal front was also evident in the 300 m temperature analysis (Fig. 12).

The analysis of the wind velocity component perpendicular to the cross section (u, the 250° component) in Fig. 19 shows the highest speeds at low levels, below 2 km. Speeds above 30 m s^{-1} were found at the top of the boundary layer beneath the lower boundary of the front. The front was a zone of large horizontal and vertical shear in u that exceeded 15 m s^{-1} (10 km)$^{-1}$ and 10 m s^{-1} km^{-1}, respectively. Reference to the 300 m traces (Fig. 17) shows the rapid changes in meteorological variables as the NOAA aircraft flew across the front between 14.33 and 14.36 GMT.

The relative vorticity $-\partial u/\partial y$ (Fig. 20) was calculated from the u-component wind analysis (Fig. 19) and shows the largest vorticities ($> 16 \times 10^{-4}$ s^{-1}) near the surface within the lower portion of the front. The vorticity decreased with height as the front broadened and the horizontal shear decreased with increasing height above the sea. Note that the vorticity within the lower portion of the front (Fig. 20), as well as the 300 m vorticity (Fig. 11), were ~ 10 times the Earth's vorticity, truly mesoscale in both dimension and magnitude.

The transverse circulation for Fig. 20, also along the line AA′ of Fig. 8 is shown in Fig. 21. The wind velocity component parallel to the cross-section (v, the 160° wind) is shown in Fig. 21a. Since the cross-frontal scale (~ 25 km) was much less than its length scale (~ 200 km), the horizontal velocity divergence (convergence) was assumed to be closely approximated by $\partial v/\partial y$. The resulting divergence (Fig. 21b) contained a narrow band of convergence that extended upward from the surface within the frontal zone, with the largest values of $\sim -13 \times 10^{-4}$ s^{-1} below 300 m. A zone of divergence was situated above the low-level convergence along the warm side of the front. The cross-frontal divergence was of comparable magnitude to the vorticity. The divergence was vertically integrated through the continuity equation to obtain the vertical velocity (Fig. 22c) which shows strong mesoscale shows strong mesoscale ascent of ~ 1 m s^{-1},

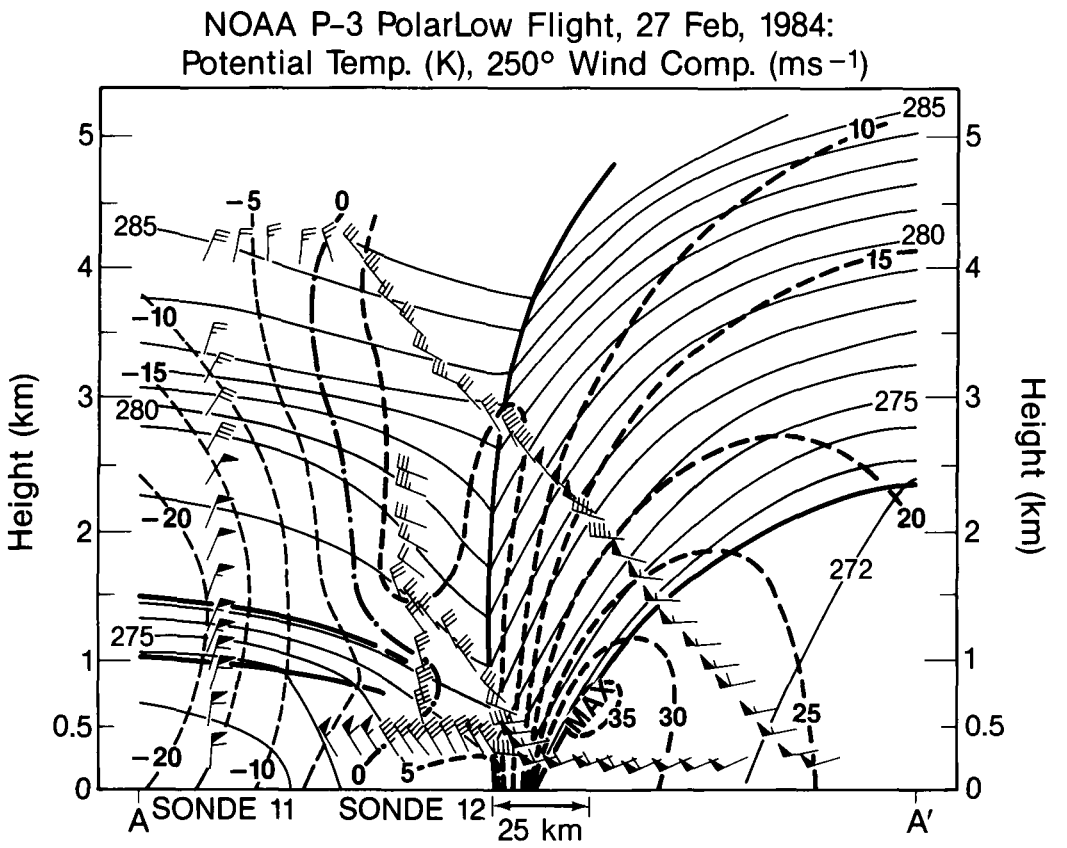

Fig. 19. Cross-section analysis of potential temperature (K, thin solid lines) and the 250° wind velocity component, i.e., the wind component perpendicular to the cross section (m s^{-1}, heavy dashed lines; positive, the zero line; a heavy dash-dot line, and thin dashed lines; negative) along the cross-section projection line AA′ of Fig. 8 at 13.40 GMT 27 February 1984. Frontal and stable-layer boundaries are indicated by the solid lines. NOAA aircraft wind vectors and dropwindsonde wind profiles are wind vectors with flags and barbs that are the same as indicated in Fig. 6.

within and toward the warm side of the front. The largest ascent was ~1.5 m s^{-1} at ~2 km above the surface. A region of sinking motion occurred above 2 km in the warmer air north of the frontal zone. The sloping zone of strong mesoscale ascent within the front was coincident with the narrow band of heavy convective precipitation, described in Subsection 5.3.

By subtracting the phase velocity of the polar low from the horizontal wind velocities about its circulation, it was possible to estimate the component of the horizontal velocity relative to the propagating low. The component of the phase velocity parallel to the cross section (11 m s^{-1}) was subtracted from the 160° wind component of Fig. 21a to obtain the relative horizontal flow perpendicular to the moving front. The sum of the relative horizontal wind component and the vertical velocity component (Fig. 21c) gave the storm-relative transverse (y,z) flow about the frontal structure of the polar low. The storm-relative transverse circulation (Fig. 21d) shows the convergence of boundary-layer air into the lower portion of the front. The air ascended along a slantwise path within the front. Descending air was ingested into the warm side of the front. The vertical circulation about the frontal precipitation band of the polar low was strikingly similar to that shown by Jorgensen (1984) for a hurricane eyewall precipitation band.

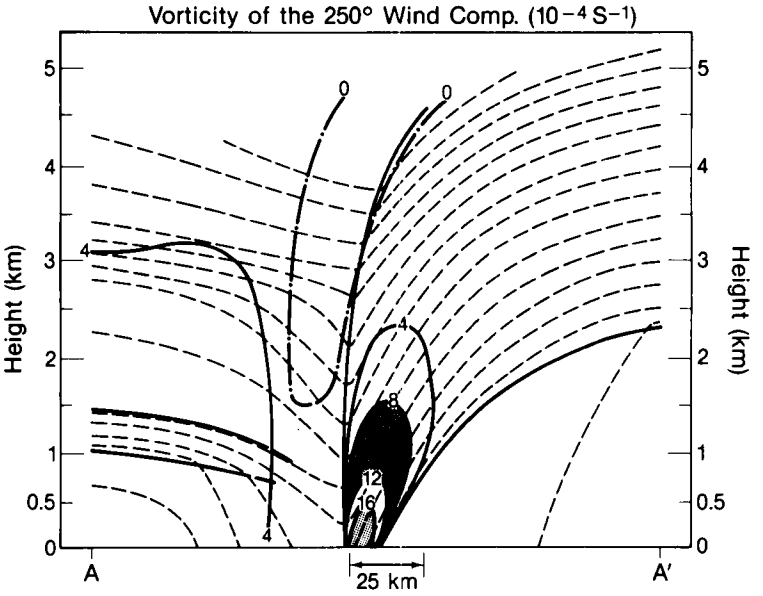

Fig. 20. Cross-section analysis of relative vorticity (10^{-4} s^{-1}) of the 250° wind velocity component of Fig. 19. Potential temperature (thin dashed lines) and frontal and stable-layer boundaries are the same as shown in Fig. 19.

The cross section of equivalent potential temperature (Fig. 22) along the line AA′ of Figs. 8 and 19 shows a layer of convective conditional instability ($\partial\theta_e/\partial z < 0$) confined to a shallow (<2 km) layer beneath the front and the capping boundary layer stable layer. The highest θ_e's below 1.5 km and the layer of largest instability occurred in the region of warmest potential temperatures (Fig. 19) and highest moisture mixing ratios on the warm side of the frontal zone. These high values of θ_e ($\theta_e > 285$ K) were implicit in the original traces of temperature T and moisture mixing ratio q (Fig. 17) where the maximum T, −0.6°C, and q, 3.0 g kg^{-1}, were measured at ~14.35 GMT during the penetration of the front and its associated asymptote in the low-level wind field. These high θ_e's were coincident with the zone of mesoscale frontal convergence and ascent (Fig. 21b and c), and the aircraft-measured 3 m s^{-1} upward vertical air motion at 14.35 GMT (Fig. 17). The relationship between the conditionally unstable, narrow zone of mesoscale ascent and the strong mesoconvective cloud systems and precipitation of the polar low is described in Section 5.3.

It is of interest to compare the vertical and horizontal distribution of θ_e for the polar low with that of a tropical cyclone. The Hawkins and Imbembo (1976) θ_e cross section for Hurricane Inez, 1966, shows an inner core of high θ_e, with the θ_e minimum at an altitude of ~5 km (500 mb), within the center of the hurricane. By comparison, the polar-low θ_e minimum within its high θ_e core (Fig. 22) occurred at an altitude of ~2 km. Similarly the depth of the hurricane layer of conditional instability at 20 km or greater distance from its center was ~4 km as compared with the same instability in the shallow 1–2 km capped boundary layer of the polar low (Fig. 22).

Absolute momentum m was defined by Eliassen (1962) in his treatment of the geostrophically forced secondary circulations in the vicinity of frontal zones. By definition

$$m = u - fy, \tag{1}$$

where u is the wind component perpendicular to the cross section, f is the Coriolis parameter, and y is distance in cross-frontal direction. Eliassen (1962) noted that in regions of strong baroclinity, such as fronts, forced circulations take the shape of ellipses, which are tilted in the direction of the sloping isopleths of m. Emanuel (1983) extended this concept to describe the effect of tilted,

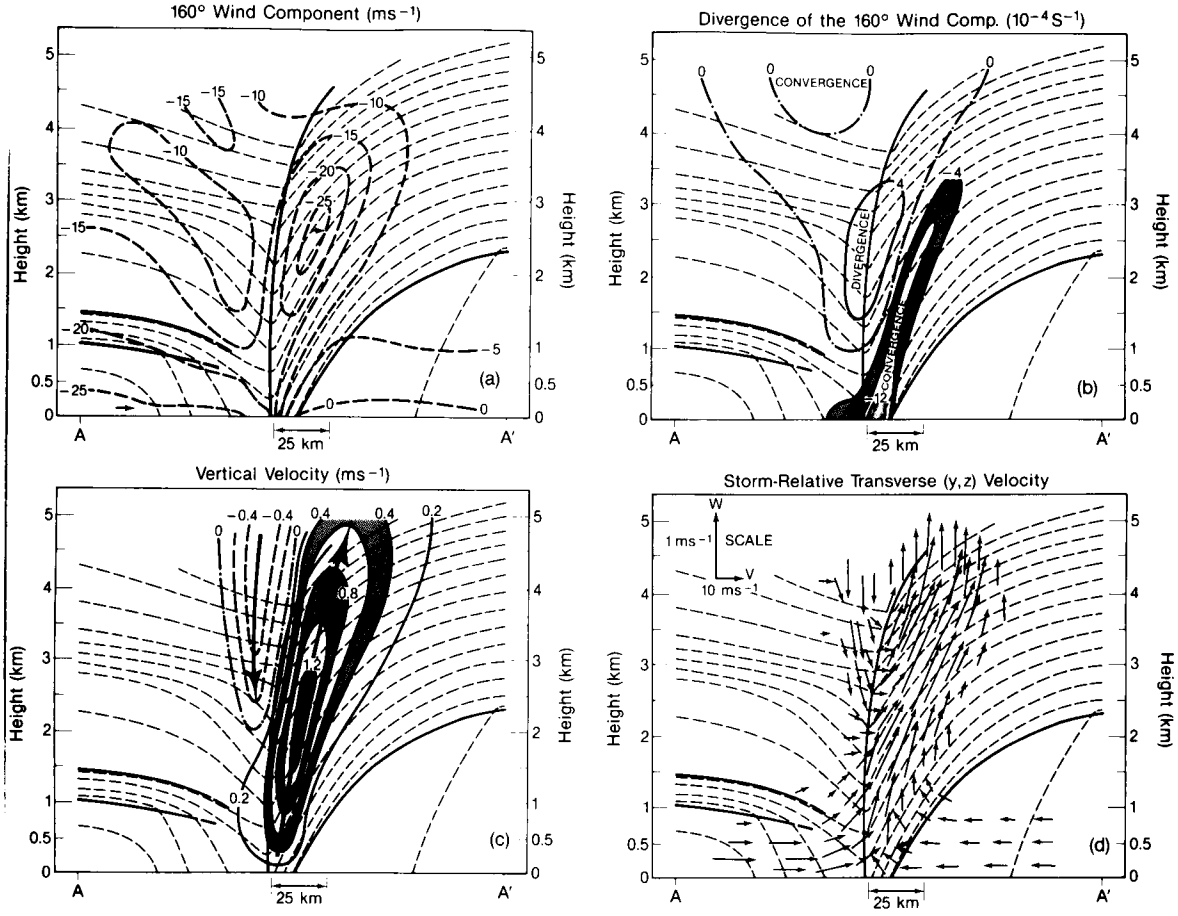

Fig. 21. Cross-section analysis of transverse circulation for Fig. 19. (a) The 160° wind velocity component, i.e., the wind component parallel to the cross section (m s^{-1}, heavy dashed lines); (b) the divergence (10^{-4} s^{-1}) of the 160° wind; (c) the vertical velocity (m s^{-1}) from the vertical integration of the divergence of Fig. 21b; (d) the relative transverse (y,z) velocity vectors (heavy arrows). Potential temperature (thin dashed lines) and frontal and stable-layer boundaries (heavy solid lines) are the same as shown in Fig. 19.

(slanted) frontal circulations upon the formation of mesoconvective instabilities. He suggested that since air parcels do not ascend vertically within baroclinic environments, one should evaluate the potential for convective instability along paths of constant m, rather than constant y.

The analysis of absolute momentum was prepared from the u-component wind of Fig. 19. The analysis (Fig. 23) shows that the maximum horizontal gradient in m coincided with the zone of highest vorticity shown in Fig. 20. The areas of maximum tilt (slope) in m were within the layer of maximum vertical shear in u, and of largest baroclinity in cross-frontal potential temperature gradient (Fig. 19). The heavy arrow vectors entered within the front (Fig. 23) are the storm-relative flow vectors from Fig. 21d. Note that the relative vectors are nearly parallel to the isopleths of m. In addition, the degree of conditional instability along the slanted, heavy-dotted m-line (Fig. 23) is greater than the conventional vertical instability because of the more rapid decrease of potential temperature with height along the slanted m-line. Reference to the θ_e analysis (Fig. 22) shows that the depth of the conditionally instability layer is greater when measured along the slanted m-lines (Fig. 23), than is measured vertically.

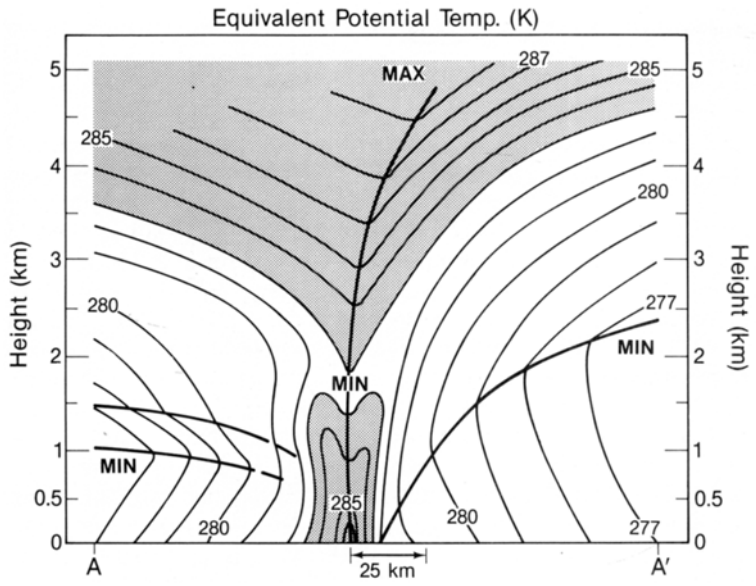

Fig. 22. Cross-section analysis of equivalent potential temperature θ_e (K, thin solid lines) for Fig.l 19. θ_e values in excess of 283 K are stippled. The frontal and stable layer boundaries are the same as those shown in Fig. 19.

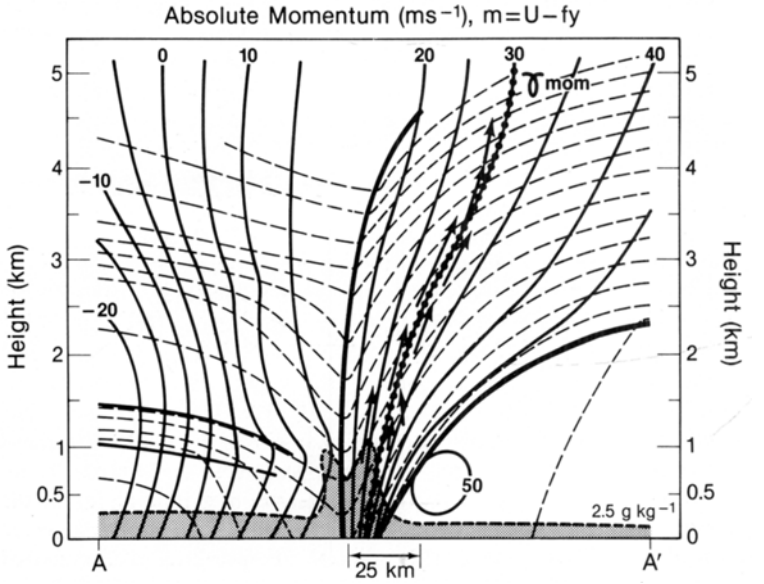

Fig. 23. Cross-section analysis of absolute momentum (m s^{-1}, thin solid lines); potential temperature (K, dashed lines from Fig. 18); 2.5 g kg^{-1} water vapor mixing ratio (heavy dashed line), with the area of mixing ratios exceeding 2.5 g kg^{-1} stippled. The 30 m s^{-1} isopleth of absolute momentum is indicated by the thin solid, dotted line. The frontal and stable layer boundaries are the same as those shown in Fig. 19.

5.3. Radar observations of convective precipitation

Radar reflectivity and Doppler radial velocity winds were measured within the precipitation of the polar low with the aircraft vertically-scanning, tail-mounted Doppler radar. The radar beam sweeps a 360° arc giving reflectivities and

radial winds in the plane perpendicular to the direction of flight. Jorgensen et al. (1983) described the NOAA airborne radar system. For the present study, we discuss our interpretation of the radar reflectivities, leaving the presentation of the Doppler wind measurements to future studies.

The most interesting precipitation echoes encountered during the flight were observed during the penetrations of the front and associated convergent asymptote southwest of the polar low center (Figs. 10, 11, 19 and 21). The radar reflectivity echoes during three penetrations are shown in Fig. 24. The first echoes (Fig. 24a) are from the second aircraft descent (Fig. 17) through the frontal convective precipitation (snow) band at 13.17 GMT. The narrow band of maximum reflectivity (>20 dBZ) sloped southeastward with increasing height. The convective precipitation was confined to a shallow layer, below 3 km, and the width of the convective element was ~6 km. We suggest that the southeastward tilt of the precipitation core with height was the result of the vertical shear in the cross-frontal wind component in the layer surface to 2.5 km, as shown in Fig. 21a. This cross-frontal vertical shear ($\partial v/\partial z$) was -10 m s^{-1} km^{-1} in the vicinity of the heaviest precipitation. The southeastward tilt in the precipitation core (Fig. 24a) is consistent with the diagnosed tilt in the frontal ascending vertical velocity plume (Fig. 21c) and the slope of the absolute momentum lines (Fig. 23) in the lowest 3 km of the front.

The strongest radar reflectivities were observed during the ~14.36 GMT penetration of the frontal precipitation band along the 300 m flight track between 14.24 and 14.45 GMT (Figs. 8, 17). The radar echo at 14.36 GMT (Fig. 24b) was observed 6 km southwest of the aircraft, after the aircraft had just passed through the precipitation band on its northwesterly track through the front and confluent asymptote of the low. This convective precipitation was ~6 km wide, and contained a narrow (~1 km), shallow (~3 km), and high-reflectivity (~45 dBZ) inner core.

Additional documentation of the coincidence of the core of heavy precipitation (Fig. 24b) with the tilted zone of maximum frontal convergence and ascent (Fig. 21) is contained in the 14.26 to 14.40 GMT aircraft measurements (Fig. 17). The bottom trace (Fig. 17) shows the downward-looking infrared radiometer temperatures. In the absence of clouds and/or precipitation in the path of the radiometer, the radiometer measured the radiative temperature of the underlying sea surface. As the aircraft approached the front and its associated convective precipitation band from the south between 14.26 and 14.28 GMT, it passed beneath the nonprecipitating, broken stratocumulus clouds contained within the ~2-km-deep boundary layer of the west-southwesterly flow in advance of the front. The sea surface was clearly visible from the 300 m flight level, and the downward-looking radiometer measured the ~2°C temperatures of the sea surface below. At 14.28 GMT, the aircraft entered light snow that fell from the overhanging anvil of the frontal precipitation band (Fig. 24a). The radiometer temperatures (Fig. 17) began to drop after 14.28 GMT, as the snow intensity increased, and began to visibly and radiometrically obscure the underlying sea surface. By 14.33 GMT, the aircraft was enveloped in heavy snow, the sea surface was no longer visible, and the radiometer measured the −2°C temperatures of the snow in the layer just beneath the aircraft. At 1434, there was only a 1.3°C temperature difference between the ambient −3.0°C temperature and the −1.7°C radiometric temperature. At 14.34:30 GMT, the snow squall abruptly abated as the aircraft reached the warm air temperatures (~−1.5°C) on the northern side of the front, and the radiometer once again had a clear view of the warm (~2°C) sea surface.

The final precipitation echoes (Fig. 24c) were observed at 15.06 GMT during the aircraft's penetration of the front on a southeasterly heading (Figs. 8, 10, 12). The penetration was nearly perpendicular to the front and its front-parallel wind component (Fig. 19). By comparison, the convective precipitation at 15.06 GMT (Fig. 24c) was shallower than that observed earlier (Figs. 24a, b), and was broken into cellular elements of ~2 km horizontal separation. None of the elements penetrated above 2 km. The front-parallel wind u was directed from right to left relative to the tilted convective cloud precipitation elements (Fig. 24c), and decreased with height ($\partial u/\partial z < 0$) within the frontal layer (Fig. 19). The tilt in the convective precipitation elements along the front was directed in the down-shear direction. Reference to Figs. 19 and

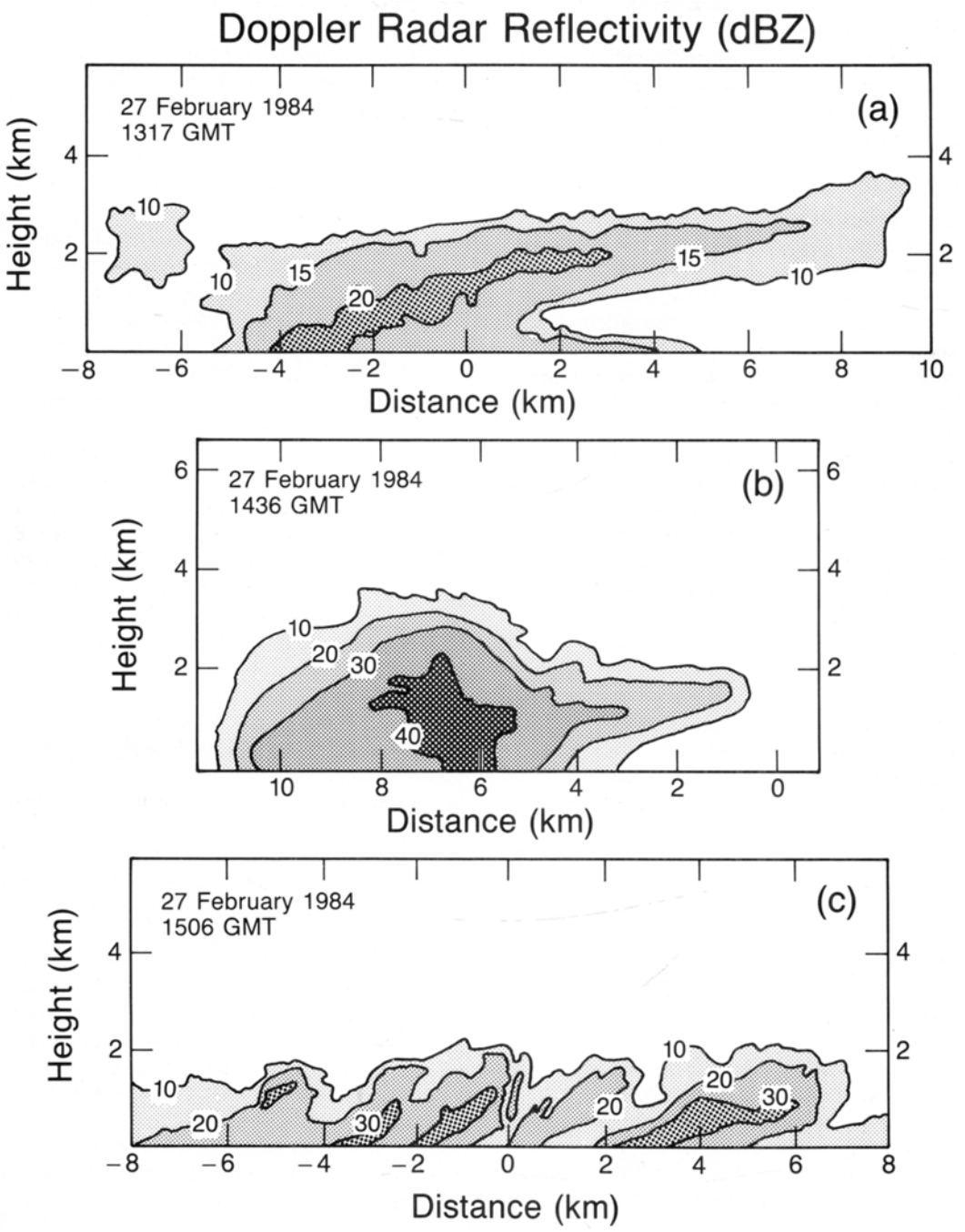

Fig. 24. NOAA aircraft tail-Doppler radar reflectivities (dBZ) that were observed during three penetrations of the primary convective precipitation band and frontal zone of the 27 February 1984 polar low. Radar reflectivities are shown for (a) 13.17 GMT, (b) 14.36 GMT, and (c) 15.06 GMT. The gradations in stippling are used to enhance the regions of greatest radar reflectivity.

21a shows significant vertical wind shear (~ 10 m s^{-1} km^{-1}) within the front in both the front-parallel and front-normal wind components. This suggests that the tilted convective precipitation elements in the vicinity of the front could have contributed to convective momentum fluxes in the lowest 2 km of the polar low. It remains for future analysis of the Doppler radar wind measurements to assess the magnitude of these convective fluxes and their possible importance in the dynamics of the polar low.

It is of interest to compare the radar reflectivity of the precipitation observed in the 27 February 1984 polar low with that measured within the convective eyewall rainband of Hurricane Allen, 1980 (see Jorgensen, 1984), both of which were observed with the same NOAA airborne Doppler radar. The vertical extent of the 10 dBZ reflectivity was much less for the polar low than for the hurricane: 3 km versus 6 km, respectively. However, the highest reflectivity values were equivalent, with both storms approaching 45 dBZ within their bands of heaviest convective precipitation.

The most significant finding revealed by the radar observations was the intensity and shallow depth and low elevation of the heavy convective precipitation within the polar low. The latent heat of condensation within the mesoconvective cloud systems of the polar low occurred within a shallow layer (below 3 km) near the sea surface.

6. Sensible and latent heat fluxes

The sea surface sensible and latent heat fluxes were estimated from the 300 m flight-level measurements of temperature T and water vapor mixing ratio q, and the radiometer measurements of sea-surface temperature T_s, and infrared sea-surface saturation water vapor mixing ratio q_s. The temperatures and mixing ratios 10 m above the sea were determined by vertical extrapolation of the 300 m measurements using the vertical descent profiles and dropwindsonde soundings. The extrapolation of the 300 m temperatures down to 10 m gave 10 m temperatures ~ 1.0 K warmer than that shown at 300 m (Fig. 12). The 10 m wind speeds $|V|$ were assumed equal to the 300 m observed values since the wind profiles showed $|V|$ either constant with the height or increasing downward toward the sea in the lowest 1 km (see Figs. 7, 16).

The bulk equations for the sea-surface (10 m) sensible and latent heat fluxes (see Kraus, 1972) are respectively given by

$$S = -\rho C_D |V|(T - T_s),$$
$$L = -\rho C_D |V|(q - q_s), \tag{2}$$

where ρ = air density, C_D = surface exchange coefficient, and the remaining variables are defined in the previous paragraph. C_D was set at 1×10^{-3} for $|V| \leqslant 10$ m s^{-1}, and increased to 2.5×10^{-3} as $|V|$ approached 35 m s^{-1}. Kraus (1972) discusses the variation of C_D as a function of $|V|$.

The 300 m water vapor mixing ratio analysis (Fig. 25) shows the highest values, $q > 2.4$ g kg^{-1}, near the center of the polar low. Values exceeding 3.0 g kg^{-1} were found in the region of highest temperatures (see Fig. 12) west of the low center, and were as high as 3.2 g kg^{-1} in a narrow band coincident with the convergence and mesoscale ascent at the frontal zone (see Figs. 10, 12, 19, 21). The extrapolation of the 300 m mixing ratios to 10 m gave values ~ 0.2 g kg^{-1} higher than shown in Fig. 25.

The sea-surface temperatures analysis (Fig. 25b) was derived from a composite of the downward-looking radiometer temperature measurements from the NOAA aircraft and the sea-surface temperatures from the NOAA-7 and -8 polar-orbitor infrared radiometer. The sea-surface temperatures show a substantial west-east gradient over the domain of the polar low. These temperatures ranged from ~ 1°C south of Jan Mayen up to 6°C along the eastern boundary of the analysis. The air at the sea surface was assumed to be saturated, with saturation mixing ratios derived from the sea-surface temperatures. The deformation of the sea-surface temperatures beneath the polar low suggests a cyclonic entwining of warm and cold water. It was not possible to establish whether this disturbed sea-surface temperature structure resulted from wind-driven ocean currents or from vertical mixing of the upper layer of the sea by the high wind speeds of the storm.

The sea-surface sensible heat flux (Fig. 26a) shows two maxima of upward sensible heat flux northwest and southeast of the storm center, in the regions of wind speeds exceeding 20 m s^{-1}

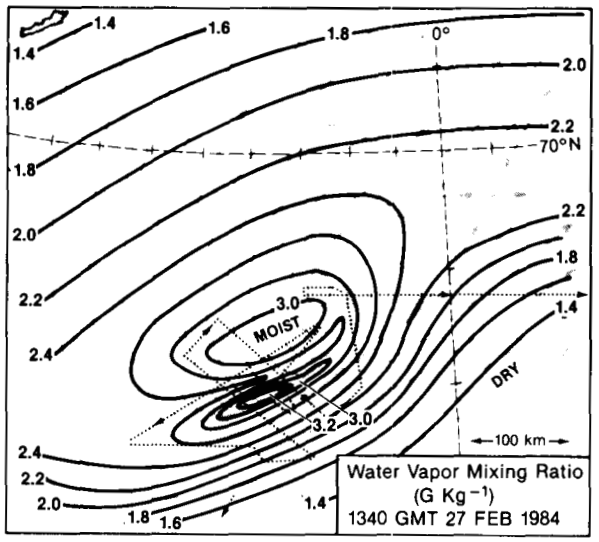

a

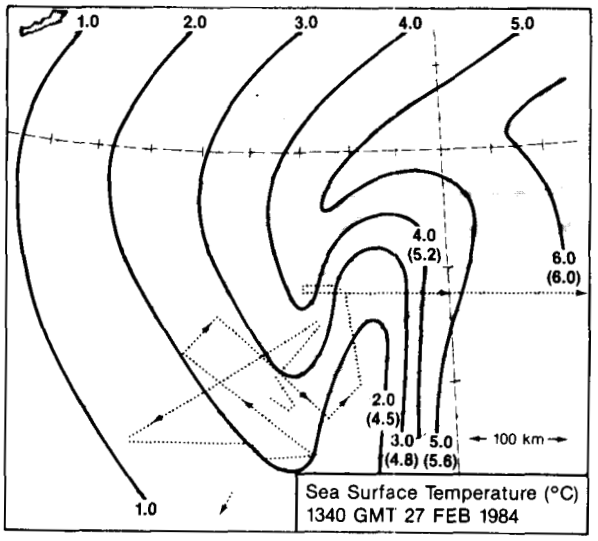

b

Fig. 25. (a) Water vapor mixing ratio (g kg^{-1}, solid lines) at 300 m at 13.40 GMT 27 February 1984. (b) Sea surface temperature (°C, solid lines) and saturation water vapor mixing ratio, same isopleths as for temperature but labeled with numbers in parentheses at 13.40 GMT 27 February 1984. Streamlines of the 300 m wind from Fig. 10a are the gray-shaded lines.

shown in Fig. 10b. Air-minus-sea temperature differences ($T - T_s$) were as high as -6°C in the regions of largest flux. The maximum sensible heat flux was 500 W m^{-2}, 1 order of magnitude greater than that for tropical cyclones (see Anthes, 1982); this was the result of the large air-sea temperature differences coupled with the high wind speeds of the polar low.

The sea-surface latent heat flux (Fig. 26b) was $\sim 10\%$ greater than the sensible heat flux (Fig. 26a) and similarly distributed about the polar low. The maximum upward latent heat flux ex-

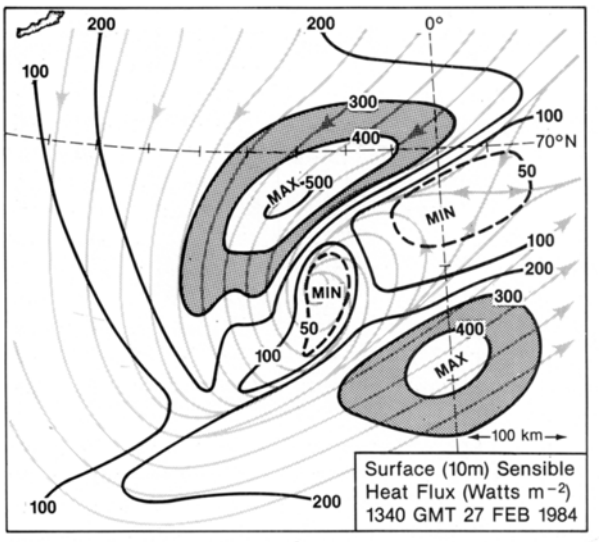

a

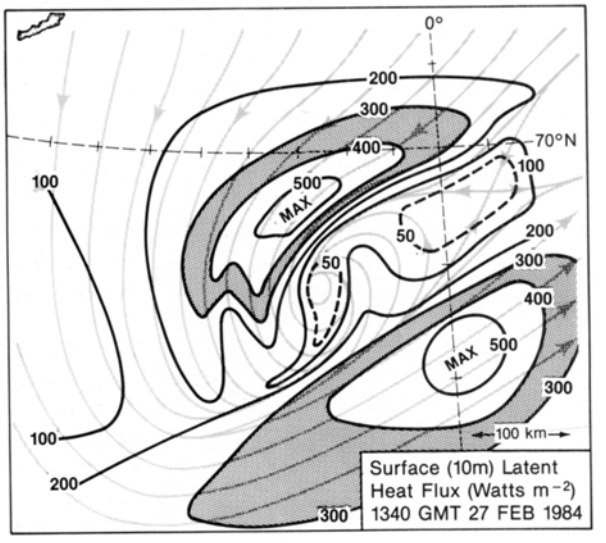

b

Fig. 26. (a) Surface (10 m) sensible heat flux (W m^{-2}, solid lines) and (b) surface (10 m) latent heat flux (W m^{-2}, solid lines) at 13.40 GMT 27 February 1984. Stippling highlights the 300 to 400 W m^{-2} flux interval. Streamlines of the 300 m wind from Fig. 10a are the gray-shaded lines.

ceeded 520 W m^{-2}, approximately one half of that for a mature tropical cyclone (see Anthes, 1982). The latent heat fluxes for the polar low were quite large considering the relatively low saturation mixing ratio (~ 5 g kg^{-1}) of the sea surface. However, the mixing ratio of the air above was significantly lower, because of its origin from off the colder and drier ice edge to the north and west, hence the large $(q - q_s) \sim 3$ g kg^{-1} that contributed to the >500 W m^{-2} of Fig. 26b. Within a tropical cyclone, q and q_s are ~ 5 times that of a polar low. The sum of sensible-

plus latent-heat fluxes from the surface below the polar low exceeded 1000 W m^{-2} in selected areas, comparable with that found within mature tropical cyclones.

7. Satellite observations

At this writing, our analysis of the satellite imagery is incomplete, and therefore we present only a limited number of the available images to illustrate the cloud structure and polar low evolution during the period bracketing the NOAA aircraft measurements. Our first discussion of the temporal continuity of the cloud structures is from the 4 km resolution, gridded NOAA-7 and -8 polar-orbiting images archived at the US National Environmental Satellite Data, and Information Service (NESDIS). Additional non-gridded 2 km resolution images received at the Tromso, Norway, telemetering station are also shown.

At 07.25 GMT 27 February 1984 (Fig. 27a) there were three adjacent cloud features of interest within the NOAA satellite images: the cyclonic cloud circulation between Scoresby Sound at the East Coast of Greenland and the northern coast of Iceland (see geography in Fig. 1), and the two adjacent convective cloud clusters southwest and southeast of Jan Mayen. The two cumulonimbus clusters were the most-developed cloud systems, having cloud-top temperatures $\sim -55°$, which closely matched the ~ 400 mb tropopause height at Jan Mayen at 12.00 GMT 27 February 1984. This east-west-oriented aggregate of clouds was situated within the low-level cyclonic shear between the northerly flow that paralleled the Greenland ice edge and the westerly flow over Iceland. The two clusters formed at the leading edge of the cold northerly Arctic outbreak that surged southward in the eastern lee of Greenland and within the synoptic-scale ascent in advance of the propagating short wave (Figs. 2, 3). The eastern cluster developed into the polar low described in Sections 4, 5.

By 10.05 GMT (Fig. 27b), the area of the two clusters had expanded. The eastern cluster had taken on a cyclonic "comma" shape, and additional high-cloud structure was forming eastward, along the "tail" of the comma cloud system. By 12.30 GMT (Fig. 27c) dramatic changes had taken place in the cloud structure south of Jan Mayen. The high clouds associated with the western cluster had diminished considerably from that shown in Figs. 27a and b. The head of the polar-low comma cloud had developed a cloud-free inner core (eye), and the cloud shield of the comma tail continued to expand eastward toward the Norwegian coast. It was at this time that the aircraft passed through the western edge of the polar-low eye (Fig. 8) and descended through the convective cloud line southwest of the storm center. Note that the areal extent of the upper-level clouds of the polar low had doubled from that shown for the eastern cluster 5 h earlier (Fig. 27a).

The next image at 13.40 GMT (Fig. 27d) shows the cloud structure of the mature phase of the polar low. Both upper and lower level clouds completely encircled the ~ 80-km-diameter cloud-free inner eye of the storm. The clouds that formed the tail of the comma continued to expand eastward, almost reaching the northwest coast of Norway. At this time, the most active and vertically developed clouds were east of the polar-low center within the tail of the comma, in the area of synoptic-scale ascent ahead of the propagating short wave (Fig. 3). This enhanced cloud structure was the first suggestion of the development of a new circulation center east of the original polar low. The western cloud cluster of Figs. 27a, c had almost completely dissipated by 13.40 GMT (Fig. 27d).

The 2-km-resolution image (Fig. 28a) at 13.40 GMT shows the cloud systems of Fig. 27d in greater detail. In this higher-resolution image, stratocumulus cloud streets paralleled the north-northeasterly low-level flow of the cold-air Arctic outbreak, and were confined to the shallow ~ 1 km boundary layer off the Greenland ice edge. The higher (colder) cloud tops south and southeast of the polar low center were cellular cumulus clouds in the ~ 2-km-deep boundary layer within the cold southwesterly flow from off of Iceland (Figs. 12, 13). The high-level cloud elements that spiral inward into the cloud-free eye of the polar low traced the cyclonic inflow into the upper portion (5–7 km) of the vortex. This cyclonic inflow at high levels was also evident in the aircraft 580 mb wind measurement (Fig. 14). Of particular interest was the development of enhanced convective cloud structure east of the

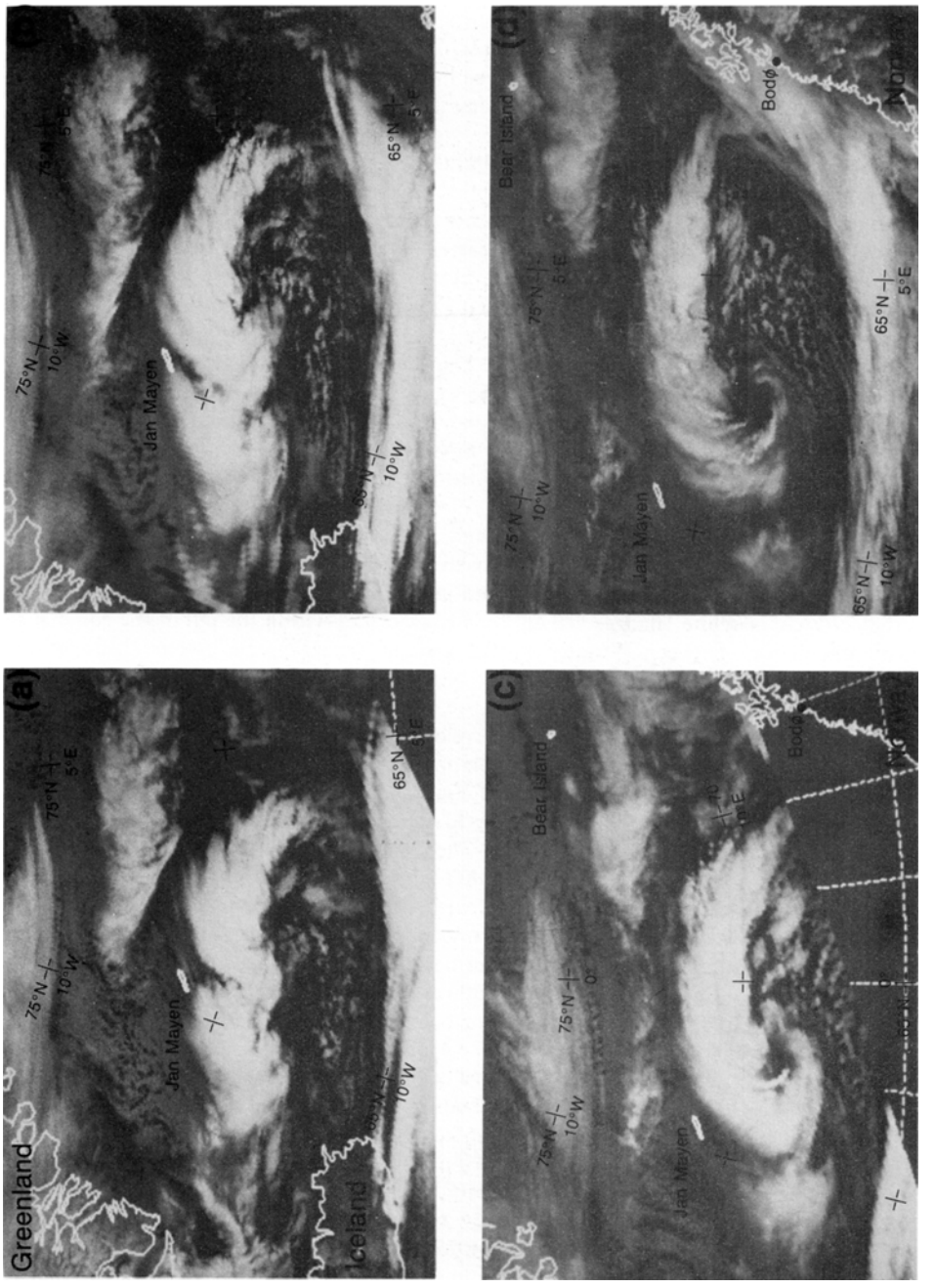

Fig. 27. NOAA-7 and -8 satellite, 4-km-spatial-resolution infrared images at (a) 07.25 GMT, (b) 10.05 GMT, (c) 12.30 GMT, and (d) 13.40 GMT 27 February 1984. The temperature scale is gray for low (warm) clouds, dark for ocean surface, and bright for high (cold) upper clouds. The geographical outlines are shown by thin white lines: The Scoresby sound area of western Greenland, upper left; Iceland, lower left; northwestern Norway, lower right; and the island of Jan Mayen, center of Fig. 27a. The distance between Jan Mayen and northwestern Iceland is ~ 600 km.

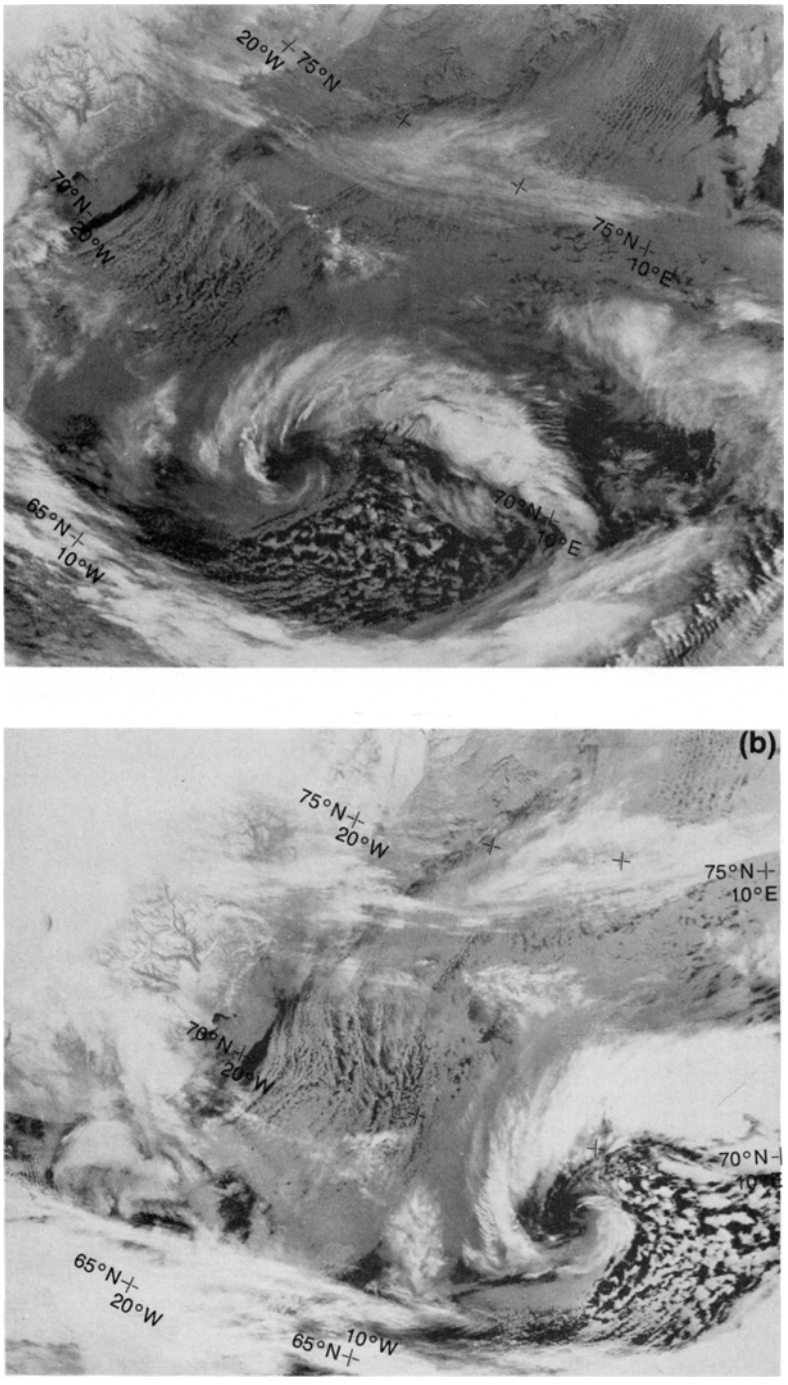

Fig. 28. NOAA-7 and -8 satellite 2-km-resolution infrared images at (a) 1340 GTM, (b) 15.24 GMT, and (c) 18.23 GMT 27 February 1984. The darkest areas are the cloud-free ocean surface and the lightest areas are high cloud tops. The ice edge of western Greenland (see Fig. 1) cuts diagonally across the upper-left-hand corner of the figures. Spitsbergen is visible in the upper-right-hand corner of Fig. 28a.

Fig. 28—continued

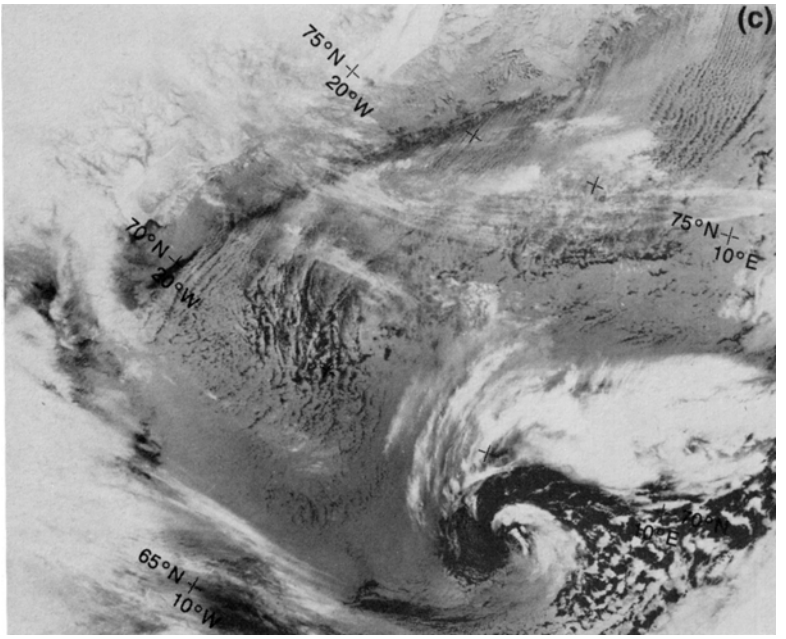

polar low within the eastern portion of its comma-shaped cloud band.

By 15.24 GMT (Fig. 28b), the eye of the polar low had expanded and was broken in its northeast sector. The image suggests that the cold surface air southeast of the low center (Fig. 12) was being drawn into the warm ($>1\,^{\circ}C$) center of the vortex. At this time, the polar low was weakening as the extensive high-cloud shield that previously encircled the low at 12.05 and 13.40 GMT had diminished in areal coverage. The major deep convective-cloud development at the time was taking place 250 km to the east of the dying storm, in the area of the tail of the comma, in association with a second polar-low cloud circulation forming downstream.

At 18.23 GMT (Fig. 28c), the eye of the original polar low had expanded further and few high clouds remained at its upper levels. The main area of deep cumulus activity had shifted east to the second polar-low development.

We summarize our analysis of the infrared satellite imagery for 27 February 1984 with nephanalysis sketches (Fig. 29) of the low-level and upper-level cloud evolutions over the period 05.18 to 18.23 GMT. This analysis depicts only the key upper- and lower-level cloud features. The uppermost sketch was derived from a DMSP satellite image, whose gray-scale temperature contour interval did not lend itself to clear reproduction for inclusion in Fig. 27. The sequence shows the decay of cyclonic cloud system 1 between 05.18 and 10.05 GMT as cloud clusters 2, and 3 expanded in area. Between 10.05 and 13.40 GMT, cluster 2 dissipated as polar low 3 formed its cloud-free inner eye. From 13.40 to 18.23 GMT, polar low 3 expanded in size and then decayed as its high cloud structure dissipated. During this same time interval, polar low 4 formed within the eastern extension of the cirrus cloud shield of polar low 3, and there was a suggestion of yet another polar-low development at 18.23 GMT to the east of polar low 4. The sequence shown in Fig. 29 suggests that downstream amplification, i.e., the triggering of new polar lows, occurred over the Norwegian Sea along the leading edge of the west-east-oriented northerly cold-air Arctic outbreak. Reference to the ECMWF analyses (Figs. 2, 3) suggests that the successive polar-low cloud circulations (Fig. 29) were triggered by the baroclinic forcing of the upper-level short wave that crossed the Norwegian Sea during the period.

Satellite measurements of total columnar ozone

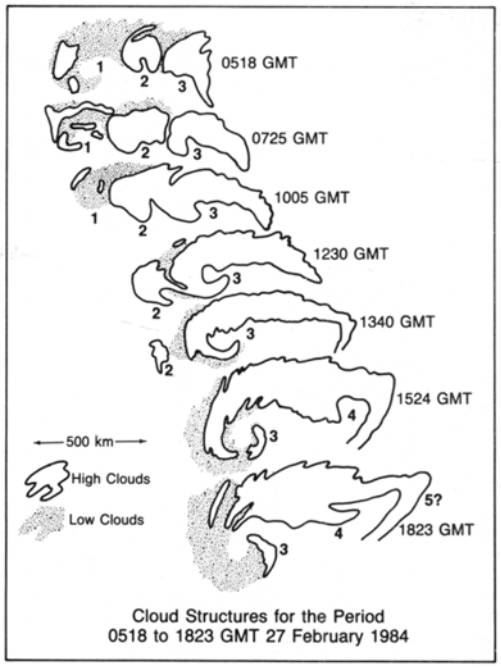

Fig. 29. Sketch of the key cloud-feature evolutions for the polar-low developments over the Norwegian Sea during the time interval 0518 to 18.23 GMT 27 February 1984. These cloud features were taken from the 4-km-resolution images of Fig. 27, plus the 05.18 GMT image (not shown in Fig. 27) and the 4-km spatial resolution 15.24 GMT and 18.23 GMT images (not shown in Fig. 27, but partially shown in the 2-km spatial resolution images Figs. 28b, c).

made with the Total Ozone Mapping Spectrometer (TOMS, described in Heath et al., 1975) were shown in Shapiro et al. (1982) to delineate the locations of jet streams and synoptic troughs and ridges near the tropopause. Shapiro et al. (1982) demonstrated that regions of high total ozone were associated with low tropopause heights at the cyclonic shear side of upper-level jet streams and within synoptic-scale cyclones and upper-level troughs. Regions of low total ozone correlated well with the high tropopause heights on the anticyclonic shear side of upper-level jet streams and within synoptic-scale anticyclones and ridges. For the present study, the TOMS measurements were analyzed to determine if significant variations in total ozone and inferred tropopause height were to be found above the polar low.

The analysis of total ozone at 12.00 GMT 27 February 1984 (Fig. 30) shows several features of interest. The highest ozone values exceeded 500×10^{-3} DBU (1 DBU = 1 atmosphere cm of total ozone). These high ozone values were associated with the low altitude of the Arctic tropopause within the upper-level trough to the east of Greenland. Tropopause heights (pressures) within the trough were 400 and 460 mb as measured in the Jan Mayen 12.00 and 18.00 GMT 27 February rawinsonde soundings, respectively. In contrast, the tropopause pressure at Bear Island, northeast of the trough and the polar low, was at 350 mb, and over the west coast of Norway, it was near 300 mb, in agreement with the low ozone amounts east of the polar low.

It is of interest to note that the polar low was situated beneath a tongue of high ozone that extended eastward along 69°N (Fig. 30). We suggest that this feature in the 12.00 GMT 27 February total ozone distribution was the result of a vertical displacement of the tropopause by the migrating upper-level short wave (Fig. 4). Future research will focus upon the relationship between migratory short waves (~1000 km wavelength or less), as observed in sequential TOMS ozone measurements, and the formation and propagation of polar lows. It should also be noted that the west-east oriented zone of maximum north-south ozone gradient (Fig. 30) south of the polar low was coincident with the similarly situated baroclinic zone at 500 mb (Fig. 2), both of which are indicative of a westerly upper-level jet stream current south of the region of polar low activity. The cyclonic curvature of the suspected jet stream cirrus band south of the polar low at the bottom of Figs. 27c, 29a coincides with the cyclonic curvature of the ozone isopleths (Fig. 30) and closely parallels the southern edge of the 500 mb baroclinic zone (Fig. 2c) and the curvature of the 500 mb trough in the height field (Fig. 2c).

8. Summary and conclusions

This paper presents the analysis of the first research aircraft observations of a polar low. The key findings from this study may be summarized as follows:

The ECMWF synoptic perspective documented that synoptic-scale, baroclinic forcing

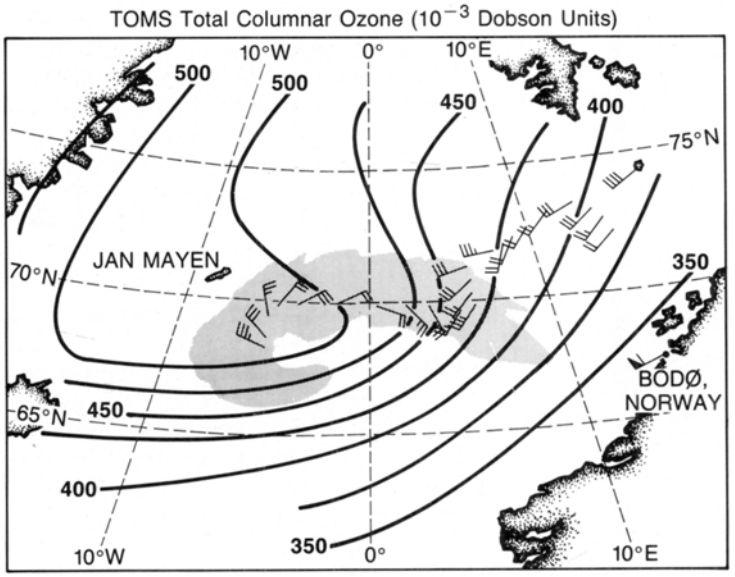

Fig. 30. Analysis of total columnar ozone (10^{-3} Dobson units) measured by TOMS, for 12.00 GMT 27 February 1984. Flight-level wind vectors are the same as those shown in Fig. 8.

was present in the region of polar-low spin up. The polar low developed within synoptic-scale rising motion and conditional instability at the leading edge of a low-level Arctic cold-air outbreak, in advance of an eastward-propagating, upper-level, short-wave trough axis, and within a synoptic-scale surface cyclone. It should be noted that the synoptic-scale environment of the polar low differed from that of the typical Norwegian Sea polar lows described by Duncan (1977, 1978), and Forbes and Lottes (1985). The Norwegian Sea polar low is said to develop in a reverse-shear, synoptic-scale flow, i.e., surface northerly to northeasterlies and upper-level southerly to southwesterlies, and propagate with the low-level flow in the direction opposite to the lower tropospheric thermal wind vector. The polar low described in the present study developed within forward-shear flow (i.e., westerlies increasing with height) and propagated eastward in the same direction as the tropospheric thermal wind vector.

The sea-level pressure at the polar-low center was 979 mb, a 17 mb deficit from the pressure 200 km from its center. The highest wind speeds ($\sim$35 m s^{-1}) were found near the sea surface, within two wind speed maxima situated in the northerly and southwesterly flow of the low. The low-level inflow into the low was primarily along two confluent asymptotes on the cyclonic shear side of the low-level wind speed maxima. The polar low possessed a warm inner core in the layer extending from the surface up to 4.2 km ($\sim$580 mb), with temperatures $\sim$5 K higher than those $\sim$200 km distant from the center. The highest water-vapor mixing ratios ($\sim$3 g kg^{-1}) were found below 1 km near the low center and within a narrow zone of strong mesoscale ascent ($\sim$1 m s^{-1}) at a mesoconvective precipitation band and associated frontal zone in the southwestern sector of the low. The 300 m equivalent potential temperature near the center of the low was $\sim$10 K higher than that $\sim$100 km from the center.

Cross-section analyses through the polar low documented the details of its internal mesoscale structure. Strong, quasi-horizontal, stable layers with bases 1 to 2 km above the sea surface, capped the neutrally stratified (adiabatic) and baroclinic marine boundary layer. The weak thermal stability and baroclinity of the boundary layer was attributed to the sensible heating of the initially cold (~ -20°C) Arctic air along its trajectory from off the Greenland coastal ice pack out over the warm (>0°C) ocean surface. Calculations of vorticity, divergence, and vertical

velocity documented the mesoscale circulations in the vicinity of the frontal zone located in the southwesterly sector of the polar low. Vorticity within the frontal zone was $\sim 20 \times 10^{-4}$ s^{-1} within a 10-km-wide band near the sea surface. The companion convergence was -13×10^{-4} s^{-1} within the zone, and the diagnosed upward vertical motion exceeded 1 m s^{-1}.

The heaviest observed precipitation was encountered in the narrow zone of maximum low-level moisture convergence and conditional instability at the primary confluent asymptote and associated frontal zone. Airborne radar measurements revealed high reflectivities, exceeding 40 dBZ, from the cumulus convection within the front, comparable in intensity with those found in mature tropical cyclones. Maximum reflectivities occurred in a shallow (2-km-deep) layer near the sea surface, indicating that the release of latent heat by the moist convection occurred at low altitude within the polar low.

Downward-looking radiometer measurements provided the sea-surface temperatures used along with 300 m temperature, water vapor, and wind measurements to determine the sea-surface sensible and latent heat fluxes into the polar low. Results showed that sensible and latent heat fluxes from the ocean surface were important components in the energetics of the polar low. The total energy flux was equally partitioned into its sensible and latent components. The maximum total flux was ~ 1000 W m^{-2}, comparable with that measured within mature tropical cyclones, though the sensible flux for the polar low was 1 order of magnitude larger than that of its tropical counterpart.

The analysis of the infrared images from the polar-orbiting DMSP, and NOAA-7 and -8 satellites revealed the complexity of the evolution of the cloud systems associated with the polar low under investigation. The images showed that the polar low was the dominant cloud circulation within a family of five polar-low cloud systems that had individual life cycles as short as 6 h. The satellite imagery for the period 07.30 GMT through 18.26 GMT 27 February 1984 showed that the aircraft began its measurements within the polar low after its peak in cumulonimbus activity. The described frontal and convective precipitation band in the southwestern sector of the polar low did not contain the major cumulonimbus cloud developments during the life cycle of the polar low. The strongest deep convective activity occurred in the northeastern sector of the low before 12.00 GMT, and shifted eastward to the new downstream polar low developments after 13.40 GMT. The observations presented herein are representative of the mature phase of the polar low, revealing its probable maximum intensity, but having been taken after the period of maximum baroclinic amplification and mesoconvective latent heating.

The structure and diagnostics of the polar low described here represent but a glimpse of one polar low derived mostly from the analysis of ~ 4 h of research aircraft measurements. Since these are the only measurements of this kind to date, one cannot say how representative they are of the structure of other polar lows. Future research will require extensive field studies to obtain continuous, multi-level measurements throughout the life cycle of a representative sample of polar lows to resolve the many remaining unanswered questions as to the triggering mechanisms and internal energetics of these fascinating and often destructive weather systems of high latitudes.

9. Acknowledgements

The authors express their thanks to the NOAA Office of Aircraft Operations for providing the research aircraft used in this study and to the flight crew and engineers whose efforts represent a major contribution to the success of the Arctic Cyclone Expedition, 1984. We also acknowledge and thank our Norwegian colleagues at The Norwegian Meteorological Institute, especially Magne Lystad and Åsmund Rabbe for their assistance during the field phase of the expedition, for providing additional observations and data sets, and for their helpful discussions of this study. We express our appreciation and thanks to Richard Reed (University of Washington) and Mike Douglas (CIRES/NOAA) for their helpful discussions of this work, and once again to Richard Reed for providing the ECMWF analyses. Our appreciation is also extended to Arlin Krueger (NASA/Goddard) for providing the TOMS ozone observations. Special thanks are extended to Mildren Birchfield for her preparation of the manuscript. This study was supported, in part, by a grant from the U.S. Office of Naval Research.

REFERENCES

Anthes, R. A. 1982. Tropical cyclones: Their evolution, structure, and effects. *Meteorol. Monogr. 5*. Boston: American Meteorological Society, 208 pp.

Bergeron, T. 1928. Uber diedreidimensional verknupfende wetteranalyse I. *Geofys. Publ. 5*, No. 6, 111 pp.

Bratseth, A. M. 1985. A note on CISK in polar air masses. *Tellus 37A*, 403–406.

Businger, S. 1985. The synoptic climatology of polar low outbreaks. *Tellus 37A*, 419–432.

Charney, J. and Eliassen, A. 1964. On the growth of the hurricane depression. *J. Atmos. Sci. 21*, 68–75.

Duncan, C. N. 1977. A numerical investigation of polar lows. *Q.J.R. Meterorol. Soc. 103*, 225–267.

Duncan, C. N. 1978. Baroclinic instability in a reversed shear flow. *Meteorol. Mag. 107*, 17–23.

Eliassen, A. 1962. On the vertical circulation in fronts. *Geofys. Publ. 24*, 147–160.

Emanuel, K. A. 1983. On assessing local conditional symmetric instability from atmospheric soundings. *Mon. Wea. Rev. 111*, 2016–2033.

Forbes, G. S. and Lottes, W. D. 1985. Classification of mesoscale vortices in polar air streams and the influence of the large-scale environment on their evolutions. *Tellus 37A*, 132–155.

Harley, D. G. 1960. Frontal contour analysis of a "polar" low. *Meteorol. Mag. 89*, 141–147.

Harrold, P. W. and Browning K. A. 1969. The polar low as a baroclinic disturbance. *Q.J.R. Meteorol. Soc. 95*, 710–723.

Hawkins, H. F. and Imbembo, S. M. 1976. The structure of a small intense hurricane—Inez 1966. *Mon. Wea. Rev. 104*, 418–442.

Heath, D. F., Krueger, A. J., Roder, H. A. and Anderson, D. B. 1975. The solar backscatter ultraviolet and total ozone mapping spectrometer (SBUM/TOMS) for Nimbus G. *Opt. Eng. 14*, 323–331.

Jorgensen, D. P. 1984. Mesoscale and convective-scale characteristics of mature hurricanes, Part II: Inner core structure of Hurricane Allen (1980). *J. Atmos. Sci. 41*, 1288–1313.

Jorgensen, D. P., Hildebrand, P. H. and Frush, C. L. 1983. Feasibility of an airborne pulse-Doppler meteorological radar. *J. Clim. Appl. Meteorol. 22*, 744–757.

Kraus, E. B. 1972. *Atmosphere-ocean interaction*. Oxford: Clarendon Press, Oxford, p. 164.

Mansfield, D. A. 1974. Polar lows: The development of baroclinic disturbances in cold air outbreaks. *Q.J.R. Meteorol. Soc. 100*, 541–554.

Mullen, S. L. 1979. an investigation of small synoptic cyclones in polar air streams. *Mon. Wea. Rev. 107*, 1636–1647.

Rabbe, Å. 1975. Arctic instability lows. *Meteorol. Ann. 6*, Norwegian Meteorological Institute, Oslo.

Rasmussen, E. 1979. The polar low as an extratropical CISK disturbance. *Q.J.R. Meteorol. Soc. 105*, 531–549.

Rasmussen, E. 1981. An investigation of a polar low with a spiral cloud structure. *J. Atmos. Sci. 38*, 1785–1792.

Rasmussen, E. 1983. A review of meso-scale disturbances in cold air masses. In *Mesoscale meteorology-theories, observations and models*, ed. D. K. Lilly and T. Gal-Chen. D. Reidel Publishing Company, Boston, 247–283.

Rasmussen, E. 1985. A case study of a polar low development over the Barents Sea. *Tellus 37A*, 407–418.

Reed, R. J. 1979. Cyclogenesis in polar airstreams. *Mon. Wea. Rev. 107*, 38–52.

Sardie, J. M. and Warner, T. T. 1983. On the mechanisms for the development of polar lows. *J. Atmos. Sci. 40*, 869–881.

Schwerdtfeger, W. and Selinger, F. 1982. *Wetterflieger in der Arktis, 1940–1944*. Motorbuch Verlag, Stuttgart, F. R. Germany, 239 pp.

Selinger, F. and Glen, A. 1983. Arctic meteorological operations and counter-operations during the World War II. *Polar Record 21*, 559–567.

Shapiro, M. A., Krueger, A. J. and Kennedy, P. J. 1982. Nowcasting the position and intensity of jet streams using a satellite-born total ozone mapping spectrometer. In *Nowcasting* (ed. K. A. Browning). Academic Press, 137–145.